MODELING OF FRICTIONAL CONTACT CONDITIONS IN STRUCTURES

A Thesis
Presented to
The Academic Faculty

By

Nguyen B. Do

In Partial Fulfillment
Of the Requirements for the Degree
Master of Science in Mechanical Engineering

Georgia Institute of Technology

August, 2005

MODELING OF FRICTIONAL CONTACT CONDITIONS IN STRUCTURES

Approved by:

Dr. Aldo A. Ferri, Advisor
School of Mechanical Engineering
Georgia Institute of Technology

Dr. Olivier Bauchau
School of Aerospace Engineering
Georgia Institute of Technology

Dr. Jerry H. Ginsberg
School of Mechanical Engineering
Georgia Institute of Technology

Date Approved: May 17, 2005

ACKNOWLEDGEMENTS

I hear and I forget. I see and I remember: I do and I understand.
- Chinese Proverb

First and foremost, I would like to thank my advisor, Dr. Al Ferri, for providing mentorship, guidance, and support for this work. His knowledge, expertise, and insights were invaluable throughout this project and have made me a better student and engineer. I would also like to thank my thesis committee members, Dr. Olivier Bauchau and Dr. Jerry Ginsberg. Lastly, my thanks to the Air Force Office of Scientific Research (AFOSR), who provided funding for this research.

My time here at Georgia Tech would not be as enriching without the support of my family and friends. Whether it was a phone call of encouragement or long study sessions, I truly thank everyone for their help and support.

TABLE OF CONTENTS

Acknowledgements iii

List of Tables vi

List of Figures vii

Summary x

Chapter 1 Introduction 1

1.1 Frictional Damping in Built-Up Structures 3

1.2 Friction Modeling and Simulation 5

1.3 Energy Transfer and Dissipation 10

1.4 Outline of Thesis 12

Chapter 2 Friction Modeling and Simulation 14

2.1 Valanis Model 15

2.2 LuGre Model 17

2.3 System Modeling and Analysis 20

2.4 Numerical Simulation Results 28

2.5 Comparison of Integration Methods 34

2.5.1 Explicit Integration Methods 35
2.5.2 Implicit Integration Methods 38

Chapter 3 Energy Transfer and Dissipation: Discrete System 42

3.1 System Model 43

3.2 System Simulation 48

3.3 Steady-State Vibration Response 49

3.4 Free Vibration Response 55

3.5 Energy Dissipation 57

Chapter 4 Energy Transfer and Dissipation: Continuous System 66

4.1 System Model 67

4.1.1 Governing Equations 68
4.1.2 System Properties 70
4.1.3 State-Space Formulation 72

4.2 System Simulation 74

4.2.1 Mode Number Convergence 75
4.2.2 Steady-State Frequency Response 77

4.3 Energy Dissipation 81

4.3.1 System Energies 82
4.3.2 Controllability of the Beam-Mass System 85

4.4 Sensitivity of the Beam-Mass System 88

4.4.1 Sensitivity to Tuning Parameter 89
4.4.2 Sensitivity to Friction Laws 91

Chapter 5 Summary and Conclusions 95

5.1 Summary 95

5.2 Conclusions and Future Work 99

References 101

LIST OF TABLES

Table 2.1	LuGre Friction Model Parameters	19
Table 2.2	Comparison of Explicit Methods	37
Table 2.3	Comparison of Implicit Methods	40
Table 3.1	Simulation Parameters	48
Table 3.2	Natural Frequencies (rad/s)	53
Table 3.3	Percentage of Energy Dissipated by the 3^{rd} and 4^{th} Dampers to the Total Energy Dissipated	64
Table 4.1	Properties for the Beam-Mass System	71

LIST OF FIGURES

Figure 1.1	Normalized friction force vs slip velocity. (a) Coulomb, (b) Sticktion, and (c) Stribeck friction laws.	6
Figure 1.2	Saturation approximation of signum nonlinearity.	7
Figure 1.3	Smooth approximation of signum nonlinearity.	7
Figure 1.4	Delayed time of the switching strategy.	9
Figure 2.1	Closed hysteresis of the Valanis friction model.	16
Figure 2.2	Description of the frictional interface in the LuGre model.	17
Figure 2.3	Hysteresis loops for the modified LuGre and the Valanis models.	20
Figure 2.4	Stick-slip system (M = 1 kg, K = 2 N/m, and U = 0.1t m).	21
Figure 2.5	LuGre function g versus y_2 using values in Table 1.	23
Figure 2.6	Maximum magnitude eigenvalue vs y_2.	28
Figure 2.7	Nondimensional position vs. τ using *ode45* with RelTol = 10^{-4} and AbsTol = 10^{-6}.	29
Figure 2.8	Nondimensional velocity vs. τ using *ode45* with RelTol = 10^{-4} and AbsTol = 10^{-6}.	30
Figure 2.9	Nondimensional bristle displacement vs. τ using *ode45* with RelTol = 10^{-4} and AbsTol = 10^{-6}.	30
Figure 2.10	Nondimensional friction force vs. τ using *ode45* with RelTol = 10^{-4} and AbsTol = 10^{-6}.	31
Figure 2.11	$\lambda_{max}(J)$ vs τ from *ode45* with RelTol = 10^{-7} and AbsTol = 10^{-7}.	32

Figure 2.12	Maximum eigenvalue during the transition from (a) microslip to macroslip and (b) macroslip to microslip.	33
Figure 2.13	Close-up of y_3 vs τ using *ode45* with RelTol = 10^{-4} and AbsTol = 10^{-6}.	34
Figure 3.1	System model of frictional contact at a connection joint.	43
Figure 3.2	Stribeck friction coefficient as a function of velocity.	45
Figure 3.3	Flow chart to calculate friction force ($P = 0$ case).	47
Figure 3.4	Modal amplitude versus generalized coordinate number for (a) Mode 1, (b) Mode 2, and (c) Mode 3.	52
Figure 3.5	RMS displacement of the 3rd mass as a function of excitation frequency ratio.	54
Figure 3.6	(a) Displacement and (b) velocity time histories of the 3-DOF system ($N = 40$N, $r = 1$).	57
Figure 3.7	Energy dissipated by the (a) entire system and (b) the 3rd and 4th dampers.	60
Figure 3.8	Energy dissipated by the 3rd and 4th dampers at $N =$ 100 N.	61
Figure 3.9	Energy dissipated by the 3rd and 4th dampers with varying mass ratios ($N = 100$ N, $t_f = 15.1$ s).	62
Figure 3.10	Energy dissipated by the 3rd and 4th dampers with varying N (mass ratio = 0.5, $t_f = 15.1$ s).	63
Figure 4.1	Beam-mass system model of a jointed structure.	67
Figure 4.2	Mode function and natural frequencies for the cantilever beam.	72
Figure 4.3	(a) Displacement and (b) velocity response at $x = L$ on the beam.	76
Figure 4.4	Magnitude of the frequency response of the beam at $x = L$.	78

Figure 4.5	Phase angle of the response of the beam at $x = L$.	78
Figure 4.6	RMS Displacement frequency response of the beam system at $x = L$.	79
Figure 4.7	Modal displacement response of the beam system.	81
Figure 4.8	Total system energy after 4.6s of free response.	84
Figure 4.9	Condition number of the controllability matrix versus tuning frequency.	87
Figure 4.10	Total system energy as a function of tuning frequency for $N = 10$ N.	89
Figure 4.11	Relative displacement versus time for two tuning frequencies.	91
Figure 4.12	Total energy remaining after 4.6s versus tuning frequency for different friction laws.	93

SUMMARY

The purpose of this thesis is to explore two aspects of modeling the behavior of joint friction in structures. The first aspect deals with the accurate and efficient simulation of a simple system that incorporates the LuGre friction law. Energy transfer and dissipation in a structural joint model is the second topic of this thesis. It is hypothesized that friction could serve to pump energy from one frequency to higher frequencies where it might be dissipated more quickly. Motivation for this study stems from the need to have accurate models of high-precision space structures. Because friction at connecting joints plays a major role in the damping capacity of the structure, a good understanding of this mechanism is necessary to predict the vibratory response and enhance the energy dissipation of the structure.

Simulation results of a dynamic system with LuGre friction show that the system is relatively well-conditioned when the slip velocity is small, and ill-conditioned for large slip velocities. Furthermore, the most efficient numerical method to simulate this system is determined to be an implicit integration scheme. To study the energy transfer and dissipation, two models of a jointed structure with friction are considered. Results from the steady-state forced responses of the two structural systems indicate that friction converted low frequency, single harmonic excitation to multi-harmonic response through internal resonances. However, differences in energy dissipation results between the models show that the response of a frictional system is highly sensitive to system parameters and friction laws. Conclusions and suggestions for future research are also discussed.

CHAPTER 1

INTRODUCTION

As the 21st century begins, new missions in space are being developed that push the limits of science and technology. Whether the mission is to explore galaxies far away or predicting tomorrow's weather, there is a need for high-tech, precision structures. These structures must meet the harsh conditions of launch and the space environment as well as operate at a high level of precision and accuracy. Therefore, disturbances and uncertainties in the dynamics of the structure can be detrimental to the performance of the spacecraft. The success of a mission depends on an accurate modeling or prediction of the uncertainties as well as a good design to minimize the effects of the disturbances.

One form of disturbance to a spacecraft is mechanical vibration in the structure. Because high levels of precision are required, vibrations along the structure are undesirable. These vibrations come from a number of sources. During deployment or positioning, vibrations can develop in large, built-up structures such as solar and sensor arrays. Other sources of vibration include machinery on the spacecraft and thermal differences along the structure. The vibrations propagate throughout the space structure and can cause a myriad of problems such as misalignment of instruments, control difficulties, structural instabilities, and component failures. Furthermore, significant amounts of time, and consequently cost, are wasted waiting for vibrations to damp down to acceptable levels. It is estimated that a robot manipulator system on a shuttle requires a time equivalent to 15 shuttle flights to damp out to an amplitude of ±1 inch [1].

Aside from reducing vibration, high precision space structures must meet stringent levels of dimensional stability. For example, NASA's next generation gamma ray telescope has strict requirements for the support structure. After deployment, the structure must get into position and remain fixed and steady within an accuracy of four millionths of an inch. Typically, other deployable structures require relatively lower levels of precision, from three to four thousandths of an inch [2]. These requirements are necessary because the support structure must function as metering structures for optical instruments. Optical instruments are highly sensitive and can even require dimensional stability to within a fraction of the wavelength of light.

To achieve high levels of precision during (and after) deployment and to reduce mechanical vibration in space structures, it is important to examine the role of friction in the structures. Specifically, friction at the connection joints in the structures is considered. During deployment, friction can be a mechanism that leads to a locking of the joint. After deployment, a microdynamic effect known as "microlurch" can occur in a structure [3]. Microlurch is a residual change in the shape of a deployed structure, which occurs after a transient dynamic event. This phenomenon can lead to the misalignment of sensitive instruments. Analytical simulations and experimental data suggest that microlurch is caused by the release of built-up strain energy within the joints and latches of a deployed structure [4]. This release of energy is an artifact of stick-slip instability due to load transfer through friction. Furthermore, it is thought that friction is the cause of small, but noticeable spontaneous vibrations in space structures [5, 6]. Although friction is the cause of microdynamic instabilities in the structure, it can also

play a positive role in the larger, global dynamics of the structure. The next section describes the role of friction in the damping capacity of large, built-up structures.

1.1 Frictional Damping in Built-up Structures

To reduce vibration in space structures, there are several solutions. One solution is to make the structure more rigid to prevent excessive vibration. However, rigid structures are expensive and heavy, which significantly increase the costs and resources necessary to launch the structure. Another way to reduce vibration is to improve the damping capacity of the space structures. This improvement could be achieved by studying the role of friction at the connecting joints in the structure.

Friction in connecting joints plays an important role in the damping capacity of built-up structures. It is estimated that as much as 90% of mechanical energy loss in space structures is due to dry friction at the connecting joints [7, 8]. Many techniques have been developed to use friction to increase damping at the joints. Ferri and Heck analytically explored damping enhancements using passive and active joints [9]. Through simulation results, Gaul and Nitsche showed an increase in damping performance using a semi-active friction damper at the joint [10]. A review of the research done on the effects of joint friction on structural damping may be found in [11].

Although there have been many studies on the effects of joint friction on damping, an accurate prediction of how much damping one can expect from a given system or design is a topic of much research. To add to the complexity of the problem, experimental evaluation of a structure's damping is difficult because the structure will operate in a zero gravity environment. In a series of experimental studies, Folkman *et al*.

found that the loss factor of a truss structure depended on the structure's orientation and the amplitude of vibration [12, 13]. Furthermore, some results showed a linear envelope of decay while others exhibited an exponential-like decay.

Because an experimental estimate of damping for a space structure is difficult, there is an emphasis on the development and simulation of analytical joint models. Although difficult, an important challenge to researchers is to develop analytical models that capture the full range of observed behaviors of joint friction. A number of researchers have developed simplified models to try to explain the complicated damping characteristics of a realistic trust structure. For example, models of a crude sleeve-joint as well as a nonlinear sleeve-joint have shown that variable normal forces in a frictional joint can give rise to mostly "linear" structural damping [14, 15]. In such cases, the free response is characterized by exponential-like (rather than linear) envelopes of decay.

Rather than focusing on characterizing the damping of a complex built-up structure, this thesis will focus on two aspects of modeling the behavior of joint friction. The first aspect deals with the analysis and simulation of an advanced friction model. Since the nature of the friction law has a significant impact on the behavior of joint friction, a good friction model is necessary to predict the dynamic and microdynamic responses of the structure. Furthermore, frictional systems are difficult to simulate due to numerical difficulties. A discussion of some friction models and simulation difficulties is presented in Section 1.2.

The second topic treated in this thesis is the phenomenon of "energy pumping" from one part of a structure to another. Moreover, the concept of energy pumping also

concerns the transfer of energy from low-frequency vibratory modes to higher frequency modes. Section 1.3 discusses these phenomena in greater detail.

1.2 Friction Modeling and Simulation

Although the concept of friction is easily understood, it is notoriously difficult to model and simulate. Many friction models contain a variety of nonlinear features such as discontinuities, hysteresis, internal dynamics, and other complications. These properties cause the friction models to be numerically stiff and therefore computationally cumbersome. For that reason, it would be advantageous to efficiently simulate a model that captures key frictional behavior from experiments and from other friction models.

Numerical difficulties associated with simulation of frictional systems are well documented [16, 17]. The basic problem is the numerical stiffness of such systems. Models of friction derived from the Coulomb friction paradigm suggest that the friction force changes "discontinuously" as the direction of interfacial slip changes. Figure 1.1 shows some typical sketches of friction force versus slip velocity. It should be noted that "sticking" of the frictional interface is characterized by zero slip velocity; therefore, it is not uncommon for the frictional interface to spend intermittent and finite periods of time at zero slip velocity, where the friction law is discontinuous.

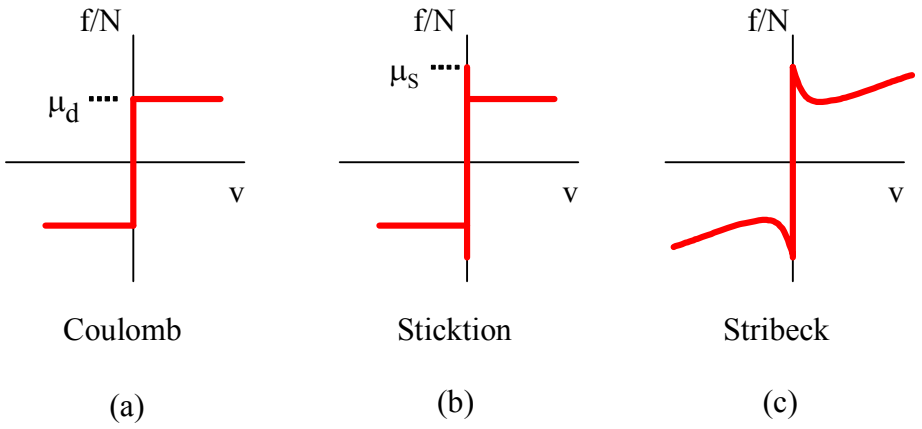

Figure 1.1. Normalized friction force vs slip velocity. (a) Coulomb, (b) Sticktion, and (c) Stribeck friction laws.

If it is assumed that the friction laws depicted in Figure 1.1 properly reflect the behavior of sliding friction, the discontinuity presents a host of analytical and computational challenges. Simulation of the time response requires very small time steps to maintain accuracy in regions where the slip velocity changes sign or where sticking occurs. Depending on the time-integration method used, it is even possible for numerical instabilities to develop. Two main strategies have been employed to deal with this problem. First, numerous studies have sought to "smooth" or "regularize" the friction law in the vicinity of the discontinuity. For example, the signum type nonlinearity depicted in Figure 1.1(a), can be replaced with a saturation-type nonlinearity, as in Figure 1.2, or a smoothly transitioning approximation as shown in Figure 1.3. In both cases, the infinite slope at zero velocity is replaced with a slope of order $1/\varepsilon$, where ε is small relative to some characteristic slip velocity for the problem in question. As ε approaches zero, the numerical stiffness of the problem becomes poorer. Consequently, time-simulation of friction-damped systems that experience finite periods of sticking are

burdened with very small time steps, necessitating high computation times in order to maintain stability and/or accuracy.

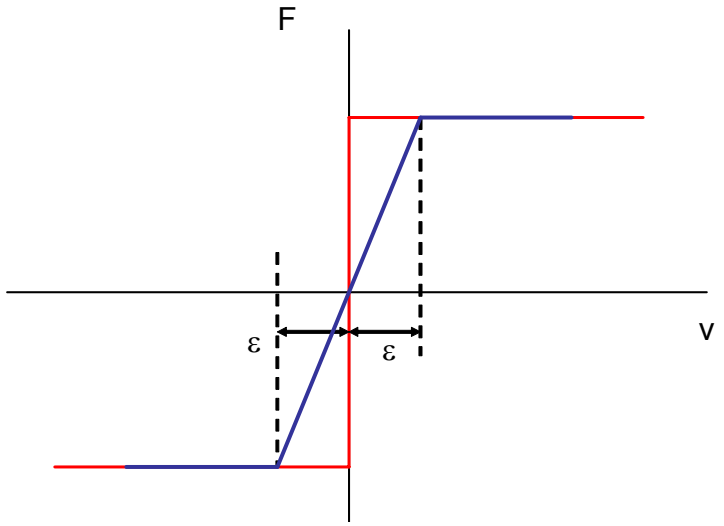

Figure 1.2. Saturation approximation of signum nonlinearity.

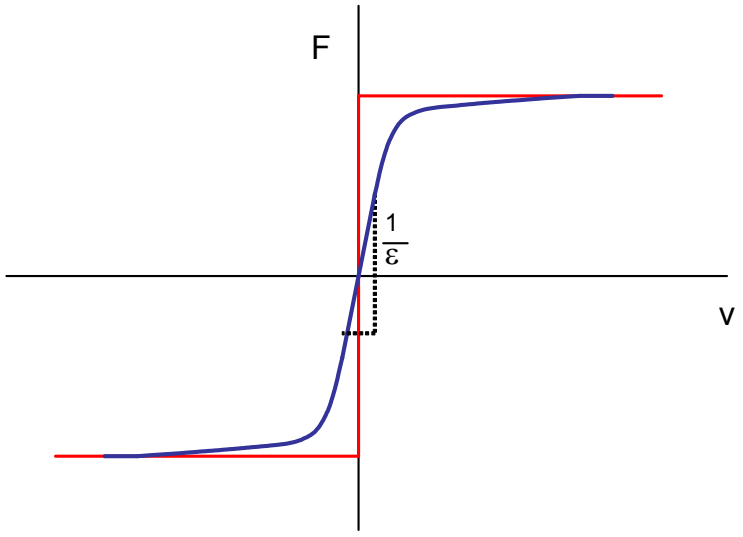

Figure 1.3. Smooth approximation of signum nonlinearity.

A second approach to address simulation of systems with discontinuous friction is to utilize a "switching strategy," or also known as an event-driven strategy [18]. In this approach, the system can be simulated using a discontinuous friction law, a saturation approximation, or a smooth approximation. However, when the slip velocity changes sign, a check is performed to determine whether the maximum-available friction force is sufficient to prevent slip from occurring [19, 20]. If the friction force is large enough to prevent slip, then a set of "sticking equations" (which model the system with a stuck interface) are integrated. Otherwise, integration of the "slipping equations" is continued. Details of this procedure are discussed in Chapter 3.

While the switching strategy alleviates the numerical stiffness problems associated with smoothing the discontinuity, another problem arises. As seen in Figure 1.4, the accuracy of the method hinges on accurate determination of the switching time. Figure 1.4 shows a transition from slipping to sticking, followed by renewed slip in the opposite direction. Due to errors in the computational solution, this switching time could be "delayed" (or "advanced") by some small amount of time. Equivalently, delays could occur due to the discrete nature of the numerical solution.

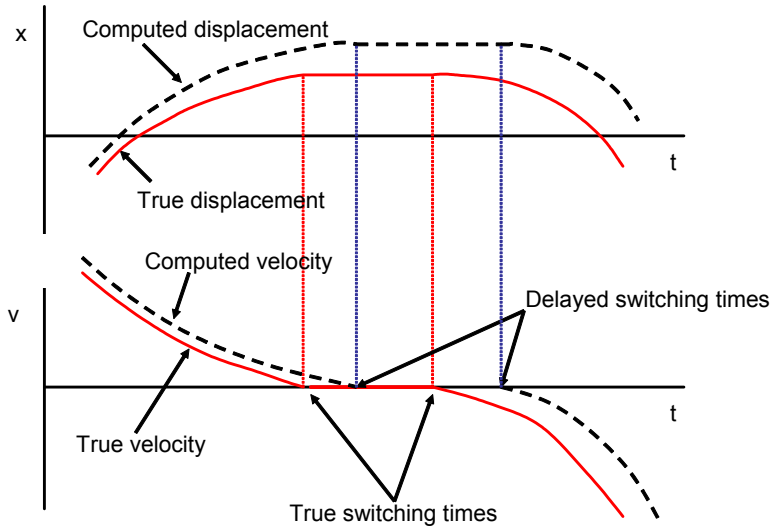

Figure 1.4. Delayed time of the switching strategy.

In reality, the physical friction process is not discontinuous. Various models of friction have been proposed that address this shortcoming by refining the behavior of the interface when the slipping velocity is small or when it changes sign. For example, "microslip" models allow small amounts of displacement to occur during sticking. A common microslip model is the Iwan-model, also termed the elastic-perfectly plastic model [21]. Conceptually, the model can be thought of as a spring in series with a Coulomb friction element having friction force μN, where μ is the coefficient of friction and N is the normal force. When the force in the spring reaches a magnitude of μN, the force in the Iwan-model saturates until the direction of slip reverses. Smooth versions of this behavior have also been proposed. Examples of friction models with smooth microslip behavior include the Dahl model [22], the Valanis model [23, 24], and the Leuven model [25, 26]. Recently, bristle models have been proposed that capture both the microslip and macroslip (sliding) regimes of interfacial friction. Haessig and Friedland proposed a bristle model where individual bristles are treated separately,

separating as bonds are broken, and then re-adhering [27]. The LuGre friction model, so named because it was developed jointly by researchers at the Lund Institute of Technology in Sweden and the University of Grenoble in France [28], is also based on a bristle interpretation of the frictional interface. However, this model treats the collection of bristles in an aggregate fashion.

The previous discussion only surveyed a small sample of the number of friction models in the literature. Applications of the friction models vary widely depending on the type and complexity of the system being simulated. Of the different friction models discussed, several have been used to study friction at structural joints. Two of the models, the Valanis model and the LuGre model, are discussed in further detail in Chapter 2. The LuGre friction model is a promising model because it captures both sticking and sliding regimes of interfacial friction. Similarly, the Valanis model shows potential because it agrees well with experimental results of friction in a joint. A comparison of the Valanis model to the LuGre model is made in Chapter 2.

Once the complexities and simulation challenges of a frictional system are understood, the effects of friction on joint behavior are investigated. The next section explores the energy transfer and dissipation due to friction at a connecting joint.

1.3 Energy Transfer and Dissipation

The second aspect of this thesis is the passive damping capabilities of joint friction. It is understood that joint friction affects damping by converting mechanical energy into heat by rubbing. Less obvious, however, it that friction can serve as a catalyst for energy pumping. The phenomenon of energy pumping is defined as the

controlled one-way transfer of vibrational energy to a passive nonlinear sink, where the energy localizes and dissipates over time [29]. Through stick-slip oscillations, it is hypothesized that joint friction can be a means to pump low-frequency vibrational energy to high-frequency vibrational energy, which can excite higher modes in the system. In a finite element simulation of a truss structure, Onoda *et al.* found that backlash nonlinearity at the joint transferred vibrational energy from lower modes to higher modes [30]. Since energy can be dissipated faster at higher frequencies, this transfer of energy to excite higher resonances may serve as a tool for increased energy dissipation. Chapter 3 explores this concept and applies it to a joint structure modeled as a simple 3 degrees-of-freedom (3DOF) system. Simulations of the steady-state and free responses of the system are performed to demonstrate the feasibility of the hypothesis.

The concepts of energy transfer and dissipation can be extended to a more complicated model. In Chapter 4, the structure is modeled as a continuous beam connected to a single degree-of-freedom (SDOF) system, with the connecting element modeled as a friction interface. An investigation of a system with a similar configuration shows the presence of internal resonances in the response of the beam [20, 31]. These internal resonances are caused by stick-slip oscillations, which excite modes at higher frequencies than the excitation frequency. In Chapter 4, the excitation of internal resonances in free and forced response is discussed. As in the 3DOF system, it is hypothesized that the vibrational energy transferred to the higher modes should dissipate faster. Simulation of the responses of the beam system is performed to validate these claims.

1.4 Outline of Thesis

This thesis deals with two topics concerning the modeling of joint friction behavior. Discussed in Chapter 2, the first topic deals with the modeling of friction and simulation strategies for frictional systems. Furthermore, Chapter 2 explores the best and most efficient simulation strategies to simulate a simple dynamical system with LuGre friction. Numerical difficulties associated with the LuGre model are examined by looking at the eigenvalues and time constants of the linearized system. With a better understanding of the dynamics of the system, the performances of several numerical integration schemes are evaluated. These schemes include both explicit and implicit numerical methods.

The second topic concerns the energy transfer and dissipation in systems with a frictional interface. Chapters 3 and 4 explore these concepts by simulating the responses of jointed structures modeled as dynamical systems. In Chapter 3, the energy transfer among subsystems of a discrete, 3DOF system is studied. Additionally, a parametric analysis of the energy dissipation in the system is performed by tuning one of the subsystems to the stick-slip frequencies. Chapter 4 extends the results of Chapter 3 to a jointed structure represented by a continuous model. Likewise, the responses of this system are simulated to study the energy transfer and dissipation. Furthermore, Chapter 4 examines the sensitivity of the frictional system to changes in system parameters. Lastly, concluding remarks as well as recommendations for future studies and research are made in Chapter 5.

The research presented in this Thesis provides a framework to study the behavior of joint friction. The selection and accurate simulation of a friction law could lead to a

more precise evaluation of the performance of a space structure. Application of the studies in Chapters 3 and 4 could serve as a preliminary guide to model and simulate specific joint structures. Ultimately, it would be desirable to develop design rules that lead to enhanced damping levels of the global structural system.

CHAPTER 2

FRICTION MODELING AND SIMULATION

Friction plays an important role in the dynamics of large, built-up structures such as space structures. Specifically, dry friction at connecting joints contributes to the majority of the damping capacity of the system. Furthermore, joint friction can lead to the locking of joints during deployment of booms and contribute to microdynamic instabilities after deployment. Since the nature of the friction law has a significant impact on the behavior of joint friction, a good friction model is necessary for the design, control, and analysis of the system.

Simulation difficulties in frictional systems are caused by the numerical stiffness of the systems. The stiffness is especially pronounced when the friction force changes discontinuously as the velocity of the slip interface changes direction. As discussed in Chapter 1, the problem can be somewhat alleviated through the use of "smoothed" versions of the friction law and/or adapting a switching strategy. However, this chapter explores an alternate approach.

In reality, the discontinuity in the friction law is an artifact that originates from modeling simplifications. Chapter 1 mentioned several more complicated friction models that have been proposed to capture the true interfacial forces in both regimes of microslip and macroslip. These models allow the transition between microslip and macroslip to be smooth and not discontinuous. They include the Dahl model, the Leuven model, the Valanis model, and the LuGre model; the later two are investigated in this chapter. The LuGre model is promising because it contains key features from other friction models

and it captures both sticking and sliding regimes of interfacial friction. The Valanis model is promising because it agrees well with experimental results of friction at a joint.

In this chapter, a description of the Valanis and LuGre friction models is given first. Secondly, a simple dynamic model is proposed to analyze the characteristics of the LuGre friction model. This model is then modified slightly to compare the LuGre friction model to the Valanis model. Next, the governing equations of the LuGre model are analyzed by using nondimensional terms and observing the dynamics of the linearized system. The dynamic system is then simulated using several explicit and implicit numerical integration techniques. Finally, conclusions are made concerning the most efficient technique to simulate the LuGre friction model.

2.1 Valanis Model

Often, the selection of a friction model is motivated by an observed response in a system. In one study, the force-displacement hysteresis response in a bolted lap joint was represented using the Valanis friction model [23]. Comparisons between experimental and simulated results showed good agreement between the Valanis model and the measured joint behavior. For the Valanis model, the rate of change in the generalized friction force, F_V, is given by

$$\dot{F}_V = \frac{e_O V\left[1+\dfrac{\lambda}{e_O}\operatorname{sgn}(V)(e_t X - F_V)\right]}{1+\kappa\dfrac{\lambda}{e_O}\operatorname{sgn}(V)(e_t X - F_V)} \tag{2.1}$$

where X is the relative displacement, V is the relative velocity, and an overdot denotes a derivative with respect to time. The function $sgn(V)$ is the signum function and is defined as $V/|V|$ when $V \neq 0$. The dimensionless parameter λ is defined as

$$\lambda = \frac{e_O}{\alpha_O\left(1 - \kappa \frac{e_t}{e_O}\right)} \tag{2.2}$$

The stiffness parameters e_0, e_t, and α_0 can be identified from the closed hysteresis loop in Figure 2.1. The dimensionless parameter κ indicates the smoothness of the stick-to-slip transition. A value of 0.99 is for a sharp transition, whereas a value less than 0.99 cause a smooth transition. For the system shown in Figure 2.1, the κ value is 0.01.

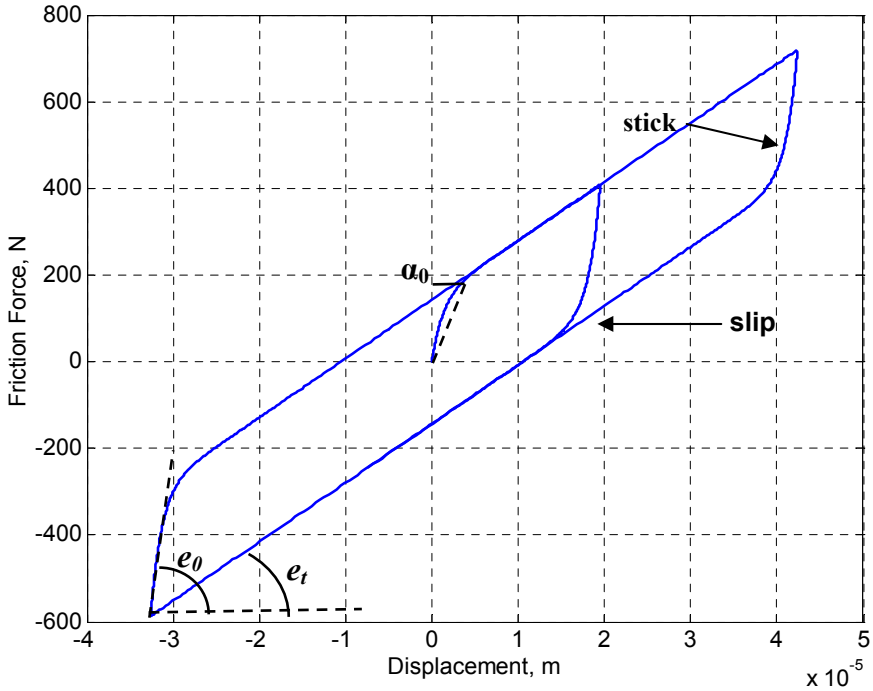

Figure 2.1. Closed hysteresis of the Valanis friction model.

2.2 LuGre Model

As discussed previously, the LuGre model has become popular because it incorporates many of the observed features of frictional behavior. For example, imbedded within the LuGre model is the Stribeck effect, displayed in Figure 1.1(c). For small levels of slip velocity, the friction force exhibits a negative derivative with respect to slip velocity. This negative slope is one of the key features of friction that contributes to limit-cycle behavior and stick-slip oscillations in frictional systems. Furthermore, the LuGre model behaves like a linear spring/damper pair when it is linearized for small motions.

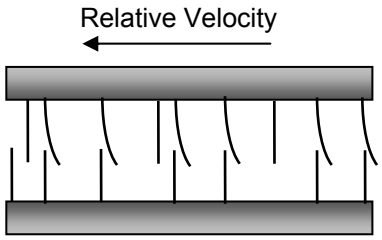

Figure 2.2. Description of the frictional interface in the LuGre model.

A qualitative description of the LuGre model is shown in Figure 2.2. At the microscopic level, two surfaces make contact at various asperities. These asperities are represented with bristles, and the bristles deflect like a spring when there is a relative velocity between the two surfaces. The deflection of the springs gives rise to the friction force. If the deflection is sufficiently large, then the bristles will slip in a highly random manner because of the irregular surfaces. Although the deflection of the bristles is

random, the LuGre model only considers the average deflection. The average deflection of the bristles, Z, is modeled by the first-order differential equation

$$\dot{Z} = V - \frac{|V|}{G(V)} Z \tag{2.3}$$

where V is the relative velocity between the two surfaces and $G(V)$ is a function that describes the Stribeck effect. The function $G(V)$ also allows the LuGre model to accommodate a higher static coefficient of friction than dynamic coefficient of friction:

$$G(V) = \frac{1}{\sigma_O}\left\{F_C + (F_S - F_C)\exp\left(-\left(V/V_S\right)^2\right)\right\} \tag{2.4}$$

where F_C is the kinetic friction force, F_S is the static friction force, σ_o is the aggregate bristle stiffness, and V_S is the Stribeck velocity. Finally, the LuGre friction force is given by

$$F_L(V, Z) = \sigma_O Z + \sigma_1 \dot{Z} + \sigma_2 V \tag{2.5}$$

where σ_1 is a damping coefficient and σ_2 accounts for viscous friction. For this study, the values used for the LuGre parameters are listed in Table 2.1. Note that V_S is a very small slip velocity, below which the frictional interface can be thought of as being "stuck" or undergoing microslip.

Table 2.1. LuGre Friction Model Parameters [28]

Parameter	Value	Unit
σ_0	10^5	N/m
σ_1	$\sqrt{10^5}$	Ns/m
σ_2	0.4	Ns/m
F_c	1	N
F_s	1.5	N
V_s	.001	m/s

As discussed in Section 2.1, the Valanis model agreed well with an experimental result of a bolted lap joint. Therefore, a comparison was made between the Valanis model and the LuGre model. However, an additional stiffness term is needed in the LuGre model because the stiffness of the bolted lap joint is included in the Valanis model, but not in the LuGre model. If a stiffness term equivalent to e_t in the Valanis model is added to the LuGre friction force in (2.5), then the LuGre model can exhibit the Valanis hysteresis loop shown in Figure 2.1. Figure 2.3 shows the hysteresis of the modified LuGre model and the Valanis model. Parameters of the LuGre model were varied to get the best fit.

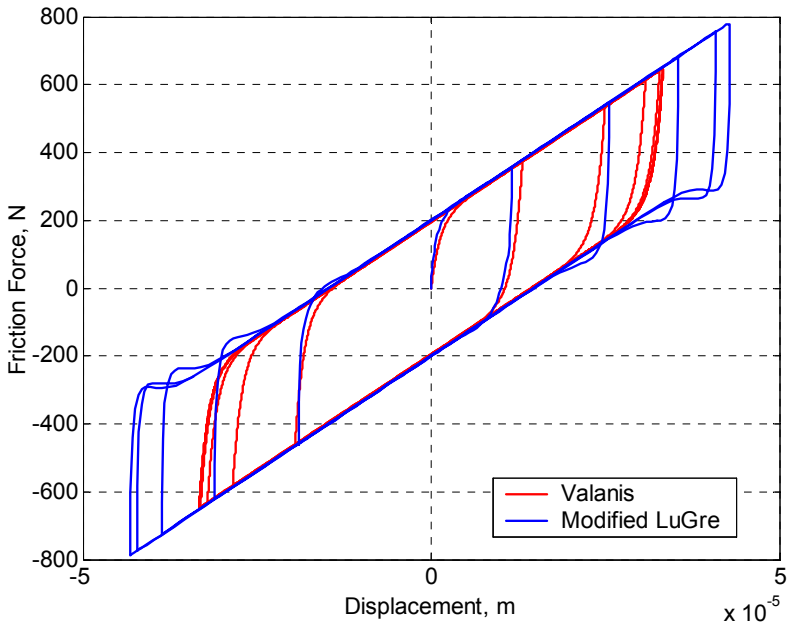

Figure 2.3. Hysteresis loops for the modified LuGre and the Valanis models.

From Figure 2.3, it is seen that the LuGre model can approximate the Valanis model well. Because the LuGre model can exhibit both classical frictional behavior (Stribeck effect) as well as experimental results, it is a good candidate for further investigation.

2.3 System Modeling and Analysis

To analyze the characteristics of the LuGre model, a system proposed by Canudas de Wit, *et al* is used to focus the present discussion [28]. The system, shown in Figure 2.4, represents a mass, M, connected to a spring K that is being pulled by a constant velocity, $\dot{U} = R$. As the mass slides along, the LuGre friction force, $F_L(V,Z)$, opposes the motion of the mass. The position of the mass is denoted by X and its velocity is V. Two first-order, differential equations govern the motion of the mass:

$$\dot{X} = V \tag{2.6}$$

$$\dot{V} = (KU - KX - F_L(V,Z))/M \tag{2.7}$$

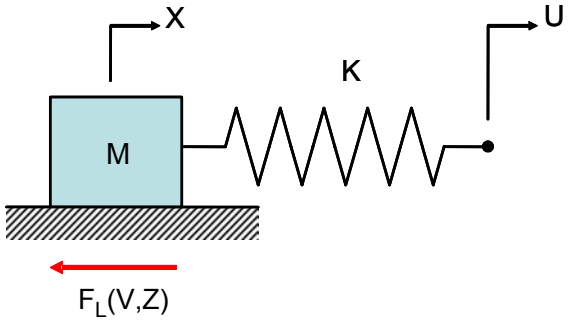

Figure 2.4. Stick-slip system (M = 1 kg, K = 2 N/m, and U = 0.1t m).

It is useful to nondimensionalize the equations governing the mass as well as that of the LuGre force by introducing the following terms:

$$y_1 = \frac{KX}{F_C},\ y_2 = \frac{V}{V_S},\ y_3 = \frac{\sigma_O Z}{F_C},\ u = \frac{KU}{F_C},\ \omega_n = \sqrt{K/M},\ \tau = \omega_n t \tag{2.8a}$$

$$\alpha = \frac{KV_S}{\omega_n F_C},\ \gamma = \frac{F_S - F_C}{F_C},\ \varepsilon = K/\sigma_0,\ s_1 = \frac{\sigma_1 V_S}{F_C},\ s_2 = \frac{\sigma_2 V_S}{F_C} \tag{2.8b}$$

There are several points to notice from the nondimensional terms. First, the time is expanded into nondimensional terms by the natural frequency of the stick-slip system. Secondly, velocity is normalized to the Stribeck velocity, which is considered to be the threshold of sticking. Microslip occurs when the $|V|$ is below V_S; and conversely, macroslip happens when $|V|$ is above V_S. Lastly, the stiffness ratio between the system and the friction model, ε (not to be confused with ε in Figures 1.2 and 1.3), is typically small due to the relatively high bristle stiffness.

When (2.8) is introduced into Equations (2.6), (2.7), and (2.3), the following three equations are obtained:

$$y_1' = \alpha y_2 \tag{2.9}$$

$$y_2' = (u - y_1 - f_L(y_2, y_3))/\alpha \tag{2.10}$$

$$\varepsilon y_3' = \alpha y_2 - \alpha \frac{|y_2|}{g(y_2)} y_3 \tag{2.11}$$

where $'$ denotes a derivative with respect to nondimensional time, τ. The friction force, F_L, and the function $G(V)$ are also converted nondimensional forms as follows:

$$f_L(y_2, y_3) = y_3 + s_1\left(y_2 - \frac{|y_2|}{g(y_2)} y_3\right) + s_2 y_2 \tag{2.12}$$

$$g(y_2) = 1 + \gamma \exp(-y_2^2)\,. \tag{2.13}$$

Equations (2.9), (2.10), and (2.11) can be conveniently represented in state-space form:

$$y' = f(y, u) \tag{2.14}$$

where y is the state vector $[y_1\ y_2\ y_3]^T$. The nondimensionalization of the terms associated with the LuGre friction model is very important. Due to the size of the bristle stiffness, the displacement Z is orders of magnitude smaller than X and V. Consequently, direct integration of the dimensional system of equations is less accurate due to round-off errors.

The analysis the dynamics of the stick-slip system began with examining the function $g(y_2)$, as shown in Figure 2.5. This function changes rapidly around $y_2 = 0$ and is approximately equal to 1 for $|y_2| > 3$. Also, the slope of g is zero at $y_2 = 0$ and is approximately zero outside the range $|y_2| > 3$. The magnitude of the slope is maximum at

$|y_2| = 1/\sqrt{2}$ (or 0.707), implying that the dynamics can change rapidly when the velocity is in the "sticking range," defined to be $|y_2| < 1$.

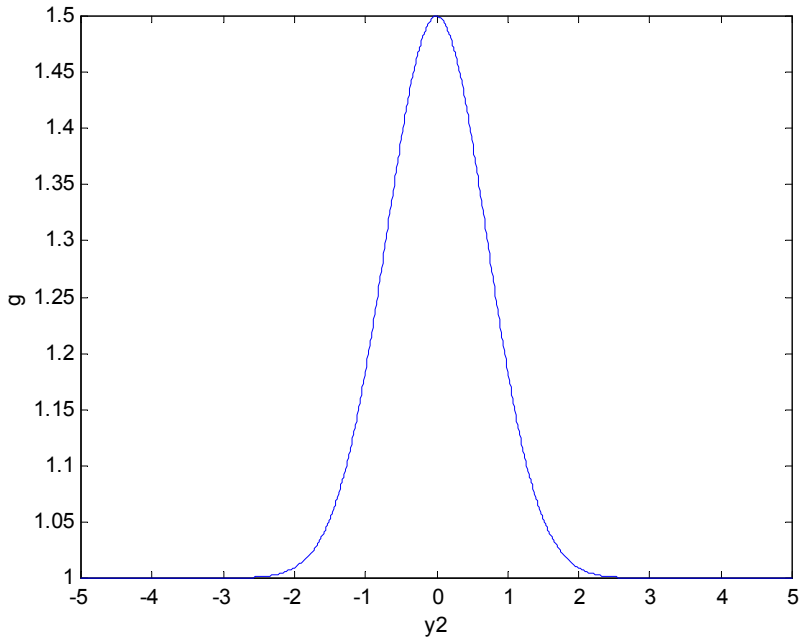

Figure 2.5. LuGre function g versus y_2 using values in Table 1.

It may be noted that equations (2.9), (2.10) and (2.11) are in standard, singular perturbation form [32]. Using the numerical values of Table 2.1, the stiffness ratio between the system and the friction model, ε, is equal to $2\text{x}10^{-5}$. The smallness of the parameter ε is partially to blame for the "numerical stiffness" of the system of equations. Numerical stiffness makes it difficult to simulate the response of the system because it requires very small time steps to ensure algorithm stability and accuracy. The problem is compounded when the system in question is more realistic, such as a multi-degree-of-freedom (MDOF) structure with multiple frictional interfaces. As the present system is

only single-degree-of-freedom (SDOF), it is possible to study the numerical stiffness problem analytically.

In order to examine the numerical stiffness of the LuGre dynamics, one can examine the Jacobian of the state dynamics:

$$J = \begin{bmatrix} \frac{\partial f_1}{\partial y_1} & \frac{\partial f_1}{\partial y_2} & \frac{\partial f_1}{\partial y_3} \\ \frac{\partial f_2}{\partial y_1} & \frac{\partial f_2}{\partial y_2} & \frac{\partial f_2}{\partial y_3} \\ \frac{\partial f_3}{\partial y_1} & \frac{\partial f_3}{\partial y_2} & \frac{\partial f_3}{\partial y_3} \end{bmatrix} = A + B(y_2, y_3) + C(y_2) \tag{2.15}$$

where

$$A = \begin{bmatrix} 0 & \alpha & 0 \\ -1/\alpha & -(s_1 + s_2)/\alpha & -1/\alpha \\ 0 & \alpha/\varepsilon & 0 \end{bmatrix}, \tag{2.16}$$

$$B(y_2, y_3) = \begin{bmatrix} 0 & 0 & 0 \\ 0 & s_1 y_3/\alpha & 0 \\ 0 & -\alpha y_3/\varepsilon & 0 \end{bmatrix} \left\{ \frac{g + 2\gamma y_2^2 \exp(-y_2^2)}{g^2} \right\} Sgn(y_2), \tag{2.17}$$

and

$$C(y_2) = \begin{bmatrix} 0 & 0 & 0 \\ 0 & 0 & s_1/\alpha \\ 0 & 0 & -\alpha/\varepsilon \end{bmatrix} \left\{ \frac{|y_2|}{g} \right\}. \tag{2.18}$$

Because the Jacobian characterizes the local, linearized dynamics of a system, it is useful in analyzing the source of the numerical stiffness when (2.14) is time integrated. If the Jacobian was evaluated at each instant in time, insight can be gained into the local dynamics of (2.14), which would be of prime importance in numerical simulations. In particular, the eigenvalues of J are important because they represent the poles of the

dynamic system. These values determine how fast the system is behaving, and therefore the maximum allowable time step to integrate the system.

In the case of explicit numerical integration routines, the stability of the algorithm depends on the size of the nondimensional time step, h. The maximum allowable time step is inversely proportional to the largest magnitude eigenvalue of J. As seen in (2.16), A has no dependence on the state vector y. From (2.17), the negative term in the exponential function causes B to become independent of y_2 for sufficiently large $|y_2|$. However, B is still dependent on the sign of y_2. The matrix C, however, grows linearly with $|y_2|$, dominating matrices A and B for high slip velocities ($|y_2| >> 10$). Thus, an expression for the largest magnitude eigenvalue of J that holds asymptotically as $|y_2|$ gets larger and larger can be derived based on the nonzero eigenvalue of C:

$$\lambda_{\max}(J) = \frac{\alpha|y_2|}{\varepsilon \; g} \tag{2.19}$$

It is seen that λ_{max} grows linearly with $|y_2|$. Therefore, as the velocity of the mass becomes large compared to the Stribeck velocity, V_S, the maximum allowable time step becomes smaller. It is also seen that λ_{max} is inversely proportional to $\varepsilon = K/\sigma_0$. Thus as the aggregate bristle stiffness σ_0 grows larger, the numerical stiffness problem worsens, especially during episodes of high slip velocity. In dimensional terms, $\lambda_{max}(J) = V\sigma_0/F_c$ sec^{-1}.

An alternate interpretation of (2.19) is obtained by inspection of the LuGre dynamics (2.11). If, over a small interval, the nondimensionalized velocity (y_2) is assumed to be constant, then the coefficients of (2.11) are constant over this interval as well. Subsequently, (2.11) becomes a linear first-order differential equation with a time constant, T_c:

$$y_3' = \frac{\alpha}{\varepsilon} y_2 - \frac{\alpha}{\varepsilon} \frac{|y_2|}{g(y_2)} y_3 = \frac{\alpha}{\varepsilon} y_2 - \frac{y_3}{T_c} \tag{2.20}$$

where

$$T_c = \frac{\varepsilon g}{\alpha |y_2|} \ . \tag{2.21}$$

From (2.21), it is evident that the time constant is equal to the inverse of the maximum eigenvalue given by (2.19). For very low values of y_2, the time constant is very large, indicating very slow friction dynamics. As the velocity emerges from the sticking range, $|y_2| \approx 1$, g falls off rapidly, decreasing the time constant. For $|y_2| > 3$, $g(y_2)$ is approximately 1 and T_c decreases inversely to y_2. As the time constant tends to zero, the dynamics of the friction model are much faster than that of the mechanical system. Qualitatively, this behavior can be attributed to the movement of the bristles. During microslip, the bristles move in a slow, linear manner. When the critical limit is reached, the bristles "snap" back to place and cause an increase in the speed of the friction dynamics. As the velocity increases, the frequency of contact between the bristles increases, therefore causing the bristles to move faster. The difference between the speed of the friction dynamics and that of the mass-spring-system is what leads to numerical stiffness. This difference results in the requirement of small time steps and the associated long computation times.

During sticking, which corresponds to small values of both y_2 and y_3, the eigenvalues of J are given by A alone. By inspection, one eigenvalue of A is identically zero. Using the friction parameters of Table 2.1, K = 2 N/m, and M = 1 kg, the remaining two eigenvalues are -111.94 ± 193.57i, which correspond to a magnitude of $\lambda_{max}(J)$ =

223.61 and a damping ratio of 0.50. For small-to-moderate values of y_2, one must compute $\lambda_{max}(J)$ numerically. Due to the presence of B, λ_{max} is a function of both y_2 and y_3. Also note that the matrix B describes sensitivity of the Jacobian to the high slope of the function g within the range $|y_2| < 1$. Figure 2.6 shows $\lambda_{max}(J)$ versus y_2 for $y_3 = \pm 1$. Also shown is the asymptotic expression for $\lambda_{max}(J)$ given by (2.19). For small velocities, the bristle displacement y_3 produces a difference in the maximum eigenvalue from the asymptotic result. However, as $|y_2|$ increases, this difference becomes less and less significant when viewed as a percentage of $\lambda_{max}(J)$.

A number of conclusions can be drawn from Figure 2.6. It is seen that the system is relatively well conditioned for low velocities ($|y_2| < 3$), including the microslip region. The system becomes more and more ill-conditioned as the slip velocity grows. This is in stark contrast to the regularization schemes portrayed in Figures 1.2 and 1.3. When the discontinuity is smoothed in the vicinity of the zero-slip point, the system of equations are ill-conditioned for small velocities (microslip) and become better conditioned as the slip velocity increases in magnitude.

This contrast may appear at first to be counterintuitive, because it is at odds with the behavior of standard approaches of friction modeling and simulation discussed in Chapter 1. Whether one smoothes the discontinuity or uses a switching between sticking and slipping dynamical systems, the numerical problems are all located in the vicinity of *small slip velocities*. In the LuGre model of friction, sticking and near-sticking conditions are where the system is *relatively well conditioned*; ill-conditioning develops as the slipping velocity gets larger.

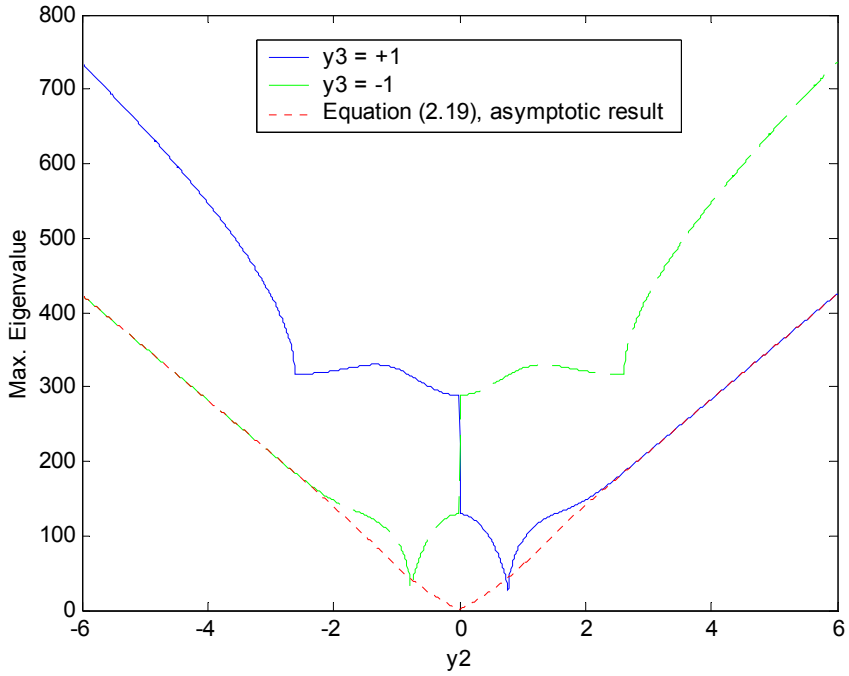

Figure 2.6. Maximum magnitude eigenvalue vs y_2.

2.4 Numerical Simulation Results

To initially simulate the stick-slip system, the Matlab function *ode45* was used. The *ode45* function is based on an explicit Runge-Kutta formula, the Dormand-Prince pair [33, 34]. The routine uses a variable time step based on specified tolerances: a relative tolerance, RelTol, whose default value is 10^{-3}, and an absolute tolerance, AbsTol, whose default value is 10^{-6}. Figures 2.7 through 2.9 show the nondimensional state quantities while Figure 2.10 shows the nondimensional LuGre friction force, $f_L(y_2,y_3)$. In the case shown, the relative and absolute tolerances are 10^{-4} and 10^{-6}, respectively. Note that the friction force behaves irregularly during the stick-slip regions. This irregular behavior can be attributed to the sudden change from the static friction force to the kinetic friction force. Further examination shows that at the instant the system begins to

slip, the friction force initially decreases before increasing with increasing velocity. This phenomenon is consistent with the Stribeck effect. Lastly, like the elastic-plastic friction model, the friction force during the sticking phase acts like a linear spring.

From Figures 2.7 and 2.8, the nondimensional displacement (y_1) and velocity (y_2) are fairly smooth and accurate, with results closely matching scaled results from [28]. On the other hand, the LuGre force, shown in Figure 2.10, exhibits a noticeable "ringing" in time intervals of high slip velocity. The ringing largely disappears when the RelTol and AbsTol values are lowered to 10^{-8}.

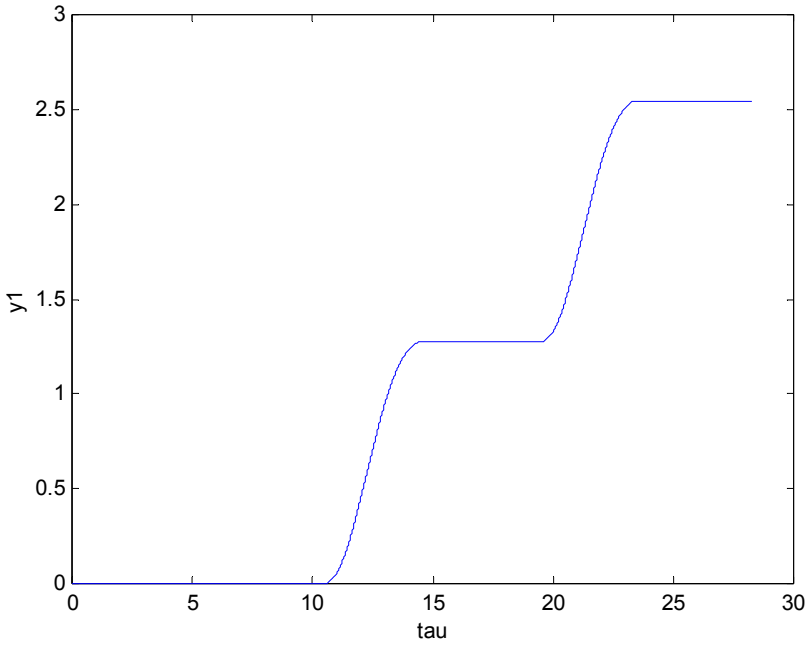

Figure 2.7. Nondimensional position vs. τ using *ode45* with RelTol = 10^{-4} and AbsTol = 10^{-6}.

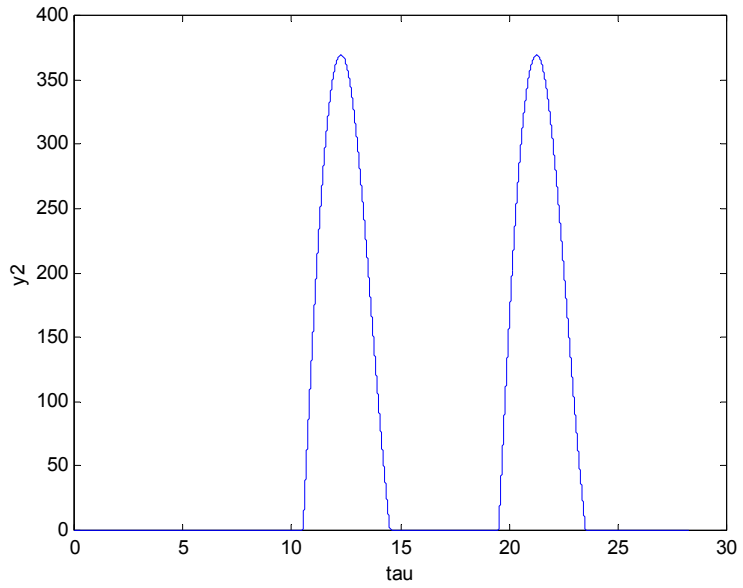

Figure 2.8. Nondimensional velocity vs. τ using *ode45* with RelTol = 10^{-4} and AbsTol = 10^{-6}.

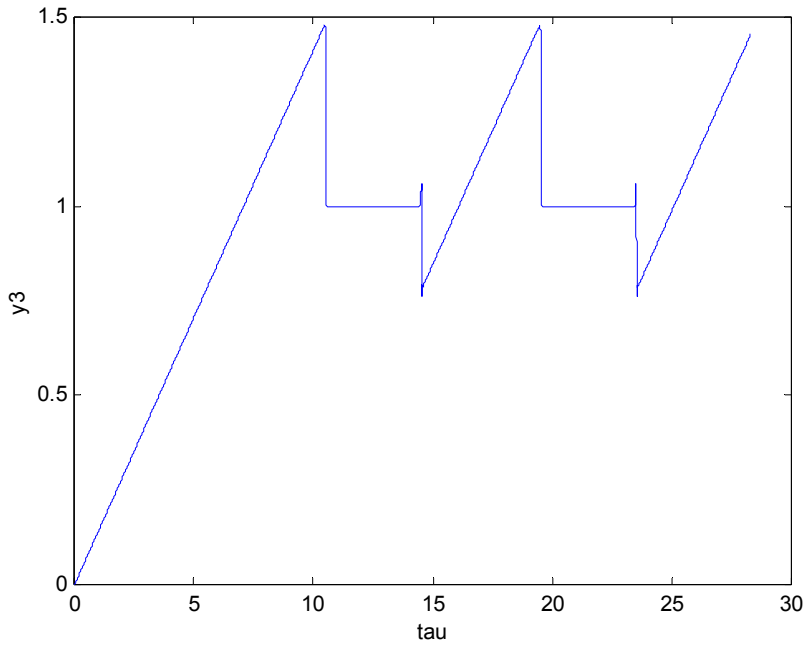

Figure 2.9. Nondimensional bristle displacement vs. τ using *ode45* with RelTol = 10^{-4} and AbsTol = 10^{-6}.

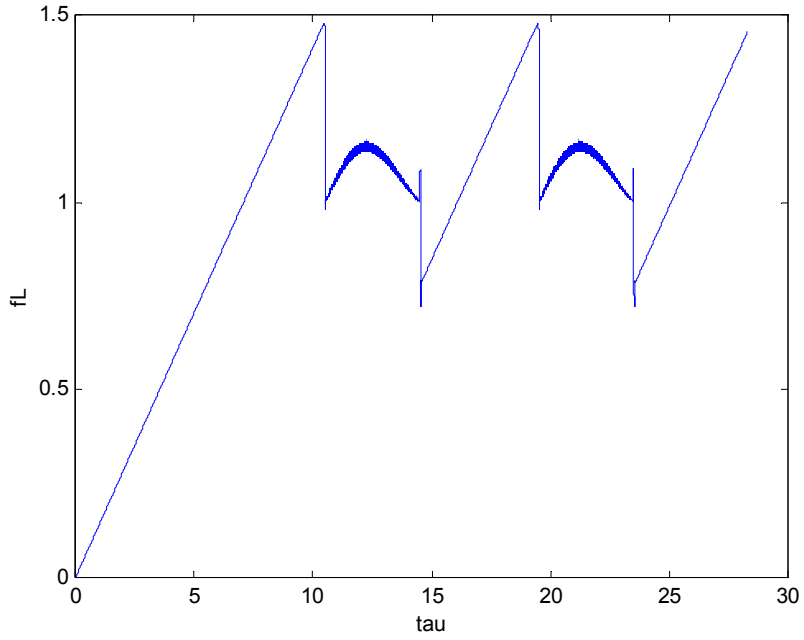

Figure 2.10. Nondimensional friction force vs. τ using *ode45* with RelTol = 10^{-4} and AbsTol = 10^{-6}.

The reason for the ringing in the friction force is uncovered by examining the Jacobian at each point along the state trajectory. Figure 2.11 shows $\lambda_{max}(J)$ versus τ from a more accurate simulation using *ode45* with RelTol = 10^{-7} and AbsTol = 10^{-7}. It is seen that the time intervals in which the largest eigenvalue magnitudes occur is closely related to occurrences of high slip velocities. Figures 2.12(a) shows a close up of λ_{max} (J) just as the mass transitions from microslip to macroslip, and Figure 2.12(b) shows λ_{max} (J) just after the first interval of macroslip comes to an end. For comparison, the figures also show the asymptotic result calculated by Equation (2.19).

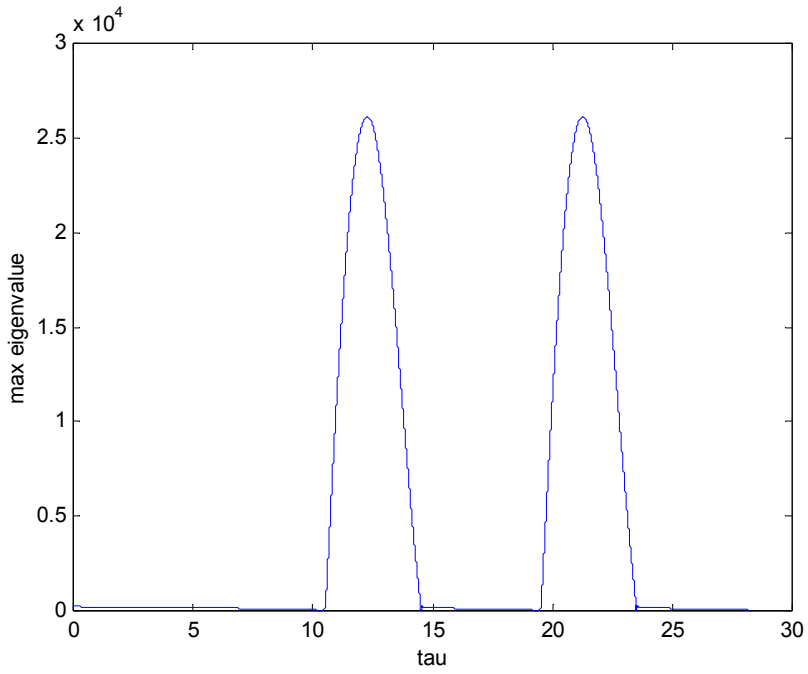

Figure 2.11. $\lambda_{max}(J)$ vs τ from *ode45* with RelTol = 10^{-7} and AbsTol = 10^{-7}.

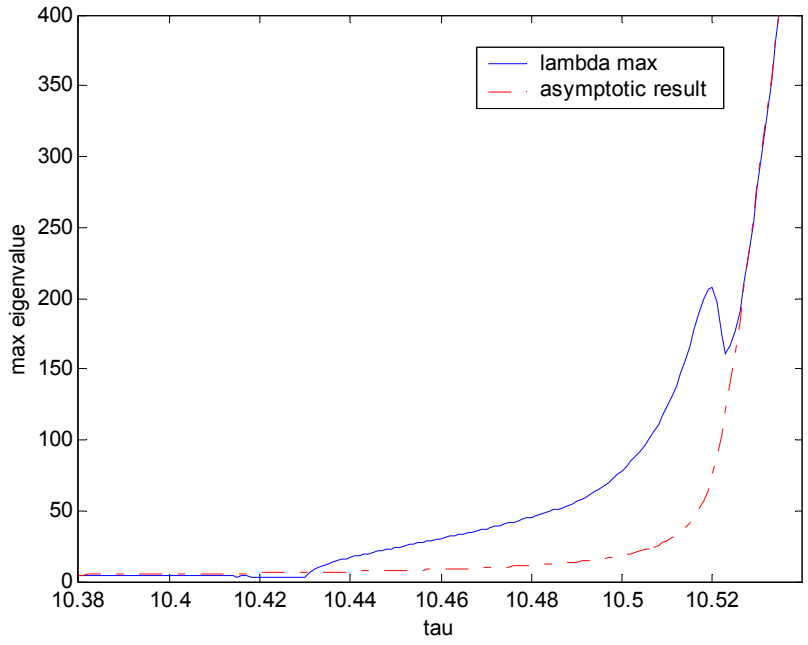

(a)

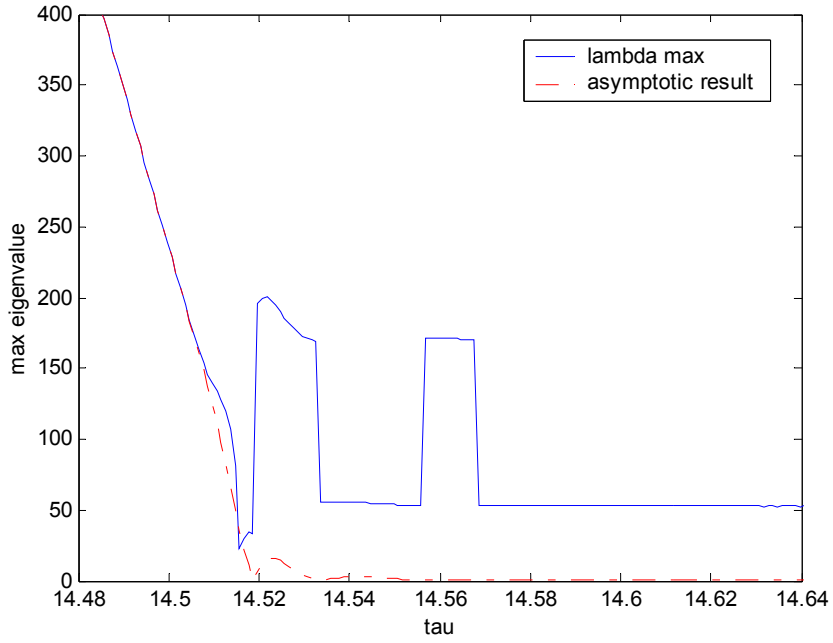

(b)

Figure 2.12. Maximum eigenvalue during the transition from (a) microslip to macroslip and (b) macroslip to microslip.

The large size of λ_{max} (J) during periods of high slip velocity is the major source of the ringing that is evident in the LuGre friction force. However, the ringing that is present in the state vector itself is far less pronounced. In fact, only the bristle displacement y_3 displays any appreciable ringing during high slip rates. Figure 2.13 shows a close up of y_3 during the period of maximum slip. It is seen that the ringing in y_3 amounts to approximately 0.01% of the nominal value. The ringing is amplified in the LuGre force because of the way that f_L is calculated; in particular, the expression in parentheses in (2.12) involves the subtraction of two terms that are large, and almost exactly equal. Operations of this type are prone to round-off errors during computation.

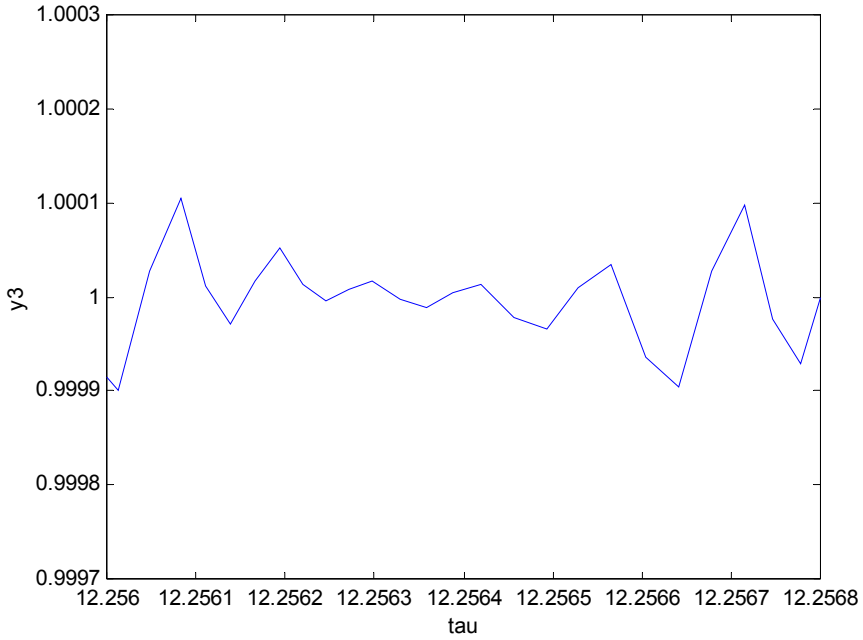

Figure 2.13. Close-up of y_3 vs τ using *ode45* with RelTol = 10^{-4} and AbsTol = 10^{-6}.

2.5 Comparison of Integration Methods

To find the best strategies to simulate the stick-slip system, several techniques were considered. Aside from using built-in Matlab functions, the techniques included user-defined explicit and implicit time integration methods. The main difference between explicit and implicit integration schemes is in the formulation. Explicit schemes use past states to define the current states, whereas implicit schemes define the current states using past and current results. Furthermore, implicit methods exhibit better stability characteristics than the explicit methods. As a note, all computer simulations were done using Matlab 6.1 on a Pentium 4, 2.4 GHz computer. Also, the simulation time was from 0 to 20 seconds.

2.5.1 Explicit Integration Methods

Although the use of a Matlab function was useful as a first attempt to solve the system, it was necessary to write a user-defined integration scheme to fully understand and control the simulation process. Because of its popularity and efficiency, the 4th order Runge-Kutta method was chosen as the explicit solver. Like the *ode45* function, this Runge-Kutta method is an explicit, time-marching scheme with a time step, h, a local error on the order of h^5, and a global error on the order of h^4 [35]. Since the maximum allowable time step is proportional to the inverse of the largest magnitude eigenvalue of the Jacobian, a time step based on this value was used for the baseline simulation. From (2.19), $\lambda_{max} = 2.62\text{x}10^4$ for the maximum value of $|y_2|$ in the simulation, which corresponds to a minimum time constant of $3.82\text{x}10^{-5}$. To best capture the dynamics of the system, a time step of 10^{-5} was used, which was more than three times less than the minimum time constant. Note that the time step used, h, is in nondimensional form defined by $h = \omega_n H$, where H is the dimensional time step.

Although the baseline simulation ($h = 10^{-5}$) gave the best results, it was not necessary to use such a small time step at all times. From previous analyses, the dynamics of the system is fast during periods of slip, but slow during microslip. Hence, it would be advantageous to base the time step based on the local dynamics of the system. One way to vary the time step was to define h based on the inverse of the maximum eigenvalue, as shown in Figure 2.11. However, this would be cumbersome because finding the eigenvalues of the Jacobian at each time step requires too many calculations. The added overhead for such a technique would be prohibitive, especially for realistic systems having a higher number of degrees of freedom.

Another way to estimate the time step necessary to simulate the system was to use the time constant, as defined by (2.21). From Figures 2.12(a) and 2.12(b), the inverse of the time constant agrees well with the maximum eigenvalue during slip. The periods where these values do not agree are the transitional periods and during sticking. However, this disagreement was addressed by setting a maximum time constant such that the integration scheme remained stable. For the system under consideration here, this maximum time constant was set at 10^{-3}. During periods of slip, estimated as $T_c < 0.02$, the time step was set to one-third of the time constant. Otherwise, the time step was set to 10^{-3}.

To make the simulation more efficient, another method based on the velocity was used to estimate the time step. Because the dynamics of the system change rapidly at the stick/stick transition periods, a small time step (10^{-4}) was used in this region. Otherwise, the time step was set to 10^{-3}. This stick-slip transition region was defined as the range $0.1 \leq |y_2| < 5$. This range was relatively conservative because it assumed that the stick-slip transition period occurred between velocities much smaller and much greater than the Stribeck velocity ($y_2 = 1$).

Table 2.2 compares the different explicit methods in order of decreasing simulation time. In addition to the baseline case (4th order Runge-Kutta with h =constant = 10^{-5}), four other cases are shown: 4th order Runge-Kutta with h switched based on the time constant, *ode45* with RelTol = AbsTol = 10^{-8}, 4th order Runge-Kutta with h switched based on $|y_2|$, and 4th order Runge-Kutta with h =constant = 10^{-3}. Two different error metrics were employed. First, the error, E, was computed by taking the absolute value of the difference in the dimensionalized friction forces at each instant in time. The

first error metric listed in Table 2 is simply the maximum of E over the duration of the simulation. The second error metric is the root-mean-squared error, E_{RMS}, and is calculated by

$$E_{RMS} = \sqrt{\frac{1}{T}\int_0^T E^2 \, dt} \tag{2.22}$$

where T is the final time. Since the number of time steps was different for each method, the data was interpolated from the baseline data set for comparison. Lastly, the simulation time is reported as a percentage to the baseline simulation time, which is 1651s, or 27.5 minutes.

Table 2.2. Comparison of Explicit Methods

Simulation Method	Time Step	Error (N)		Simulation Time (%)	Number of Steps
		Max	RMS		
Runge-Kutta (Baseline)	10^{-5}	n/a	n/a	100	2.828×10^{6}
Runge-Kutta (Time constant)	$(1/3)T_c$ or 10^{-3}	0.207	7.46×10^{-4}	14.8	4.020×10^{5}
Ode45*	n/a	1.68×10^{-4}	4.22×10^{-8}	3.62	1.476×10^{5}
Runge-Kutta (Velocity)	10^{-4} or 10^{-3}	0.320	1.30×10^{-3}	1.17	3.170×10^{4}
Runge-Kutta (Constant)	10^{-3}	3.98×10^{-4}	1.16×10^{-6}	1.14	2.829×10^{4}

* absolute tolerance = relative tolerance = 10^{-8}

Table 2.2 shows that there is a significant improvement in the simulation time by switching the time step based on the time constant of the system. However, the maximum error using this method is unacceptable (~14% error) and the number of steps required is still relatively large. The Runge-Kutta method with *h*-switching based on the velocity performed much better in terms of simulation time and number of steps, but its accuracy was the worst. The result using *ode45* had the best accuracy and a very short simulation time compared to the baseline. Finally, using the Runge-Kutta method with a constant time step of 10^{-3} produced errors comparable to the *ode45* method, but with the smallest simulation time and least amount of steps. This last result is surprising since 10^{-3} is roughly 26 times larger than the frictional time constant at the point of maximum slip velocity.

2.5.2 Implicit Integration Methods

Despite moderate successes with the explicit methods, implicit integration schemes were used to simulate the stick-slip system. The key advantage of the implicit integration methods is better stability characteristics versus the explicit methods. Therefore, it would be possible to use larger time steps (than the explicit methods) to simulate the LuGre model, even during slip. However, the disadvantage of implicit methods is the need to iterate at each time step. This iteration is necessary to solve for simultaneous equations at each time instant. Lastly, despite the improved stability characteristics, the accuracy of the implicit methods still depends upon the size of the time step.

The first implicit method to be applied to the stick-slip system was the Trapezoidal method, which is effective for solving stiff differential equations [35]. An extension of the Trapezoidal method is the Radau-IIA method [36]. Both the Trapezoidal integration scheme and the Radau-IIA scheme can be expressed in a common framework. At each time t_i, two sets of nonlinear equations must be solved for the unknown vectors, k_1 and k_2:

$$k_1 = f\left(y(t_i) + c_1 k_1 + c_2 k_2, \quad u(t_i + b_1)\right) \tag{2.23}$$

$$k_2 = f\left(y(t_i) + c_3 k_1 + c_4 k_2, \quad u(t_i + h)\right) \tag{2.24}$$

where k_1 and k_2 are 3x1 vectors that approximate in some sense the average dynamics over a time step. The value of the state vector at the next time step is expressed in terms of k_1 and k_2 as follows:

$$y(t_i + h) = y(t_i) + c_3 k_1 + c_4 k_2 \tag{2.25}$$

The difference in the Trapezoidal method and the Radau-IIA method is the values of the constants c_i and b_1. For Trapezoidal integration, the constant values are

$$c_1 = c_2 = 0, \quad c_3 = c_4 = h/2, \quad b_1 = 0, \tag{2.26}$$

and for the Radau-IIA method:

$$c_1 = 5h/12, \quad c_2 = -h/12, \quad c_3 = 3h/4, \quad c_4 = h/4, \quad b_1 = h/3 \tag{2.27}$$

For the explicit methods, various schemes were investigated for their accuracy and efficiency. Similarly, various schemes were also investigated for the implicit methods. The results of the implicit integration methods are summarized in Table 2.3. The Trapezoidal method was implemented with a constant time step of $h = 0.005$. The

Radau-IIA method was compared using three different schemes for selection of h: h = constant = 10^{-2}, h switched based on velocity, and h switched based on the time constant.

When compared to the explicit methods in Table 2.2, the implicit methods on average require less time and much fewer integration steps. The primary reason for these improvements is that larger time steps (than the explicit methods) could be used to obtain an accurate solution. Although the equations of the LuGre model are numerically stiff, the implicit integration schemes are well suited to solve them.

Table 2.3. Comparison of Implicit Methods

Simulation Method	**Time Step**	**Error (N)**		**Simulation Time (%)**	**Number of Steps**
		Max	**RMS**		
Runge-Kutta (Baseline)	10^{-5}	n/a	n/a	100	2.828×10^{6}
Trapezoidal	5×10^{-3}	0.150	7.54×10^{-4}	2.25	5.658×10^{3}
Radau-IIA (Constant)	10^{-2}	9.33×10^{-2}	4.72×10^{-4}	1.08	2.830×10^{3}
Radau-IIA (Velocity)	10^{-2} or 0.02	0.497	5.90×10^{-3}	0.56	1.436×10^{3}
Radau-IIA (Time Constant)	10^{-2} or 0.05	0.490	7.20×10^{-3}	0.47	1.216×10^{3}

Similar to the findings for the Runge-Kutta method, it is observed that the maximum error values for the variable time step methods were unacceptably large. A reason for the relatively large errors was that at the stick-slip transition regions, there was

a shift in the solution compared to the baseline. This shift occurred for both the explicit and implicit methods that used a variable time step. Since the transitions in the friction force occur very rapidly in time, even a small time shift in one simulation relative to the baseline result can give rise to relatively large maximum errors.

From Tables 2.2 and 2.3, it appears that the best choice to simulate the stick-slip system is to use the Radau-IIA method with a constant time step of 10^{-2}. Surprisingly, the use of 4th order Runge-Kutta with a constant time step of 10^{-3} also displayed a good balance between accuracy and efficiency. In terms of simulation time, both the 4th order Runge-Kutta and Radau-IIA methods are similar. The Runge-Kutta method has errors two orders of magnitude better than the Radau-IIA scheme, however, the Radau-IIA requires an order of magnitude fewer steps. Thus the best choice of integration scheme may depend on the users' preference for accuracy versus speed, as well as on the availability of computer memory. However, when simulating a large dynamical system, using a larger time step would greatly reduce the computation time. This advantage outweighs improved accuracy afforded by the Runge-Kutta method. Therefore, for large systems with LuGre friction, the Radau-IIA method appears to be the best method for numerical integration.

CHAPTER 3

ENERGY TRANSFER AND DISSIPATION: DISCRETE SYSTEM

Once the complexity and numerical difficulties associated with frictional systems are understood, an investigation into the effects of friction of the dynamics of a structural system is conducted. As discussed in Chapter 1, vibration in space structures poses a major problem because these structures have high precision and accuracy requirements. Since friction is responsible for the majority of mechanical energy loss in structures, this Chapter explores the energy dissipation caused by dry friction at a connecting joint. In particular, this study examines the ability of friction to serve as a catalyst for energy pumping. It is hypothesized that joint friction can be a means to pump low-frequency vibrational energy to high-frequency vibrational energy, through the action of stick-slip oscillations. Since energy can be dissipated faster at higher frequencies, this pumping of energy to excite higher resonances may serve as a tool for increased energy dissipation. In this manner, an inherent property of friction can be exploited to improve the overall damping capacity of the system.

A simplified model of a connecting joint with friction is presented first. The model consists of a 3 degrees-of-freedom (3DOF) spring-mass-damper system with a frictional interface. The algorithm used to calculate the friction forces and the simulation parameters are presented as well. Simulations were performed using Matlab and the equations of motion were solved using the 4^{th} order Runge-Kutta method. Next, the steady-state and free vibration responses of the system are explored, followed by a parametric study of the energy dissipation in the system.

3.1 System Model

To model the friction contact at a connection joint, a 3 degrees-of-freedom spring-mass-damper system was used. This configuration is similar to a model used by Warren to study microdynamic frictional behavior in joints [4]. The 3DOF system, shown in Figure 3.1, represents two structures modeled as single-degree-of-freedom systems that are coupled by a mass sliding against a friction surface. The sliding mass (m_2) is an order of magnitude smaller than masses m_1 and m_3. The absolute position and velocity of each mass are denoted by x_i and v_i, respectively, while the parameters k_i and c_i denote spring and viscous damping constants, respectively. Note that these variables are different than the variables introduced in the previous chapters. The function, $P(t)$, represents an external force applied to mass 1.

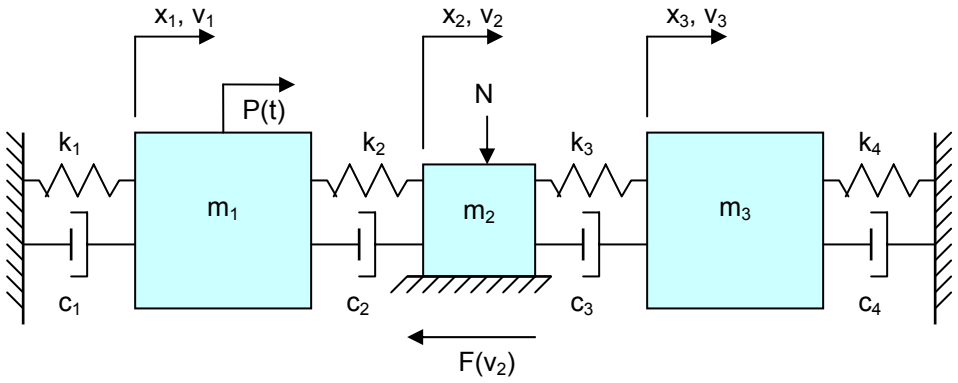

Figure 3.1. System model of frictional contact at a connection joint.

The friction force, $F(v)$, is defined as

$$F(v) = \mu N \operatorname{sgn}(v) \tag{3.1}$$

where v is the slip velocity, μ is the friction coefficient, N is the normal force, and $sgn(v)$ is the signum function where $sgn(v) = v/|v|$, $v \neq 0$. Using the Stribeck friction model, the friction coefficient, μ, is given by

$$\mu = \mu^* + \gamma(e^{-\beta|v|} - 1) + \alpha|v| \tag{3.2}$$

where μ^* is the static friction coefficient and parameters γ, β, and α are constants [37]. There is one main reason why the Stribeck friction model is used in this case instead of the LuGre model or other friction models described in Chapter 2. Because the hypothesis is that stick-slip motion pumps energy to higher modes, it is necessary to isolate this stick-slip mechanism. Continuous friction models such as the LuGre model contain other internal dynamics that may obscure the phenomenon.

Figure 3.2 shows the relationship between the Stribeck friction force and the slip velocity. The key mechanism that causes stick-slip behavior is the decrease in friction force as $|v|$ increases around zero [38]. In Equation (3.2), the parameter γ specifies the difference between the static and sliding friction coefficients while β determines the steepness of the transition. The coefficient α was set to zero because it is typically associated with a viscous-damping characteristic of lubricated contact. Setting α equal to zero allows one to distinguish between the energy dissipation by viscous damping from the energy dissipated due to dry friction.

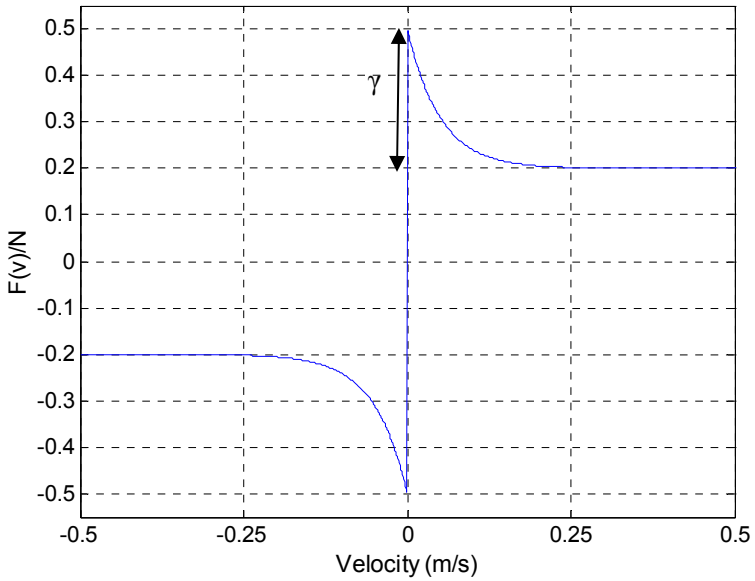

Figure 3.2. Stribeck friction coefficient as a function of velocity.

As seen in Figure 3.2, there is a discontinuity in the friction force when the slip velocity is zero. The numerical problems related to this condition are discussed in Chapter 2 as well as different methods to solve these problems. In this study, a sliding mode control (variable structure system theory) algorithm is used to handle the discontinuity and solve for the friction force [19]. This method is one of the "switching strategies" addressed in Chapter 2. Presented next is a derivation of the equations of motion and a discussion of the numerical solution technique.

The equations of motion for the 3DOF system can be written in the form

$$[M]\{\ddot{x}\}+[C]\{\dot{x}\}+[K]\{x\}=\{e_1\}P-\{e_2\}F \tag{3.3}$$

where $\{x\} = [x1\ x2\ x3]^T$, $\{e_1\} = [1\ \ 0\ \ 0]^T$, $\{e_2\} = [0\ 1\ 0]^T$, and the overdot represents a derivative with respect to time. The matrices $[M]$, $[C]$, and $[K]$ are the mass, damping, and stiffness matrices, respectively, and are defined as

$$M = \begin{bmatrix} m_1 & 0 & 0 \\ 0 & m_2 & 0 \\ 0 & 0 & m_3 \end{bmatrix}, K = \begin{bmatrix} k_1 + k_2 & -k_2 & 0 \\ -k_2 & k_2 + k_3 & -k_3 \\ 0 & -k_3 & k_3 + k_4 \end{bmatrix}, C = \begin{bmatrix} c_1 + c_2 & -c_2 & 0 \\ -c_2 & c_2 + c_3 & -c_3 \\ 0 & -c_3 & c_3 + c_4 \end{bmatrix}$$

In order to simulate the response of the 3-DOF system, the equations given by (3.3) are rewritten in the first-order, state-space form

$$\{\dot{y}\} = [A]\{y\} + \{B\}F + \{\Gamma\}P \tag{3.4}$$

where $\{y\} = [x1\ x2\ x3\ v1\ v2\ v3]^T$, $\{B\} = -[0\ 0\ 0\ ([M]^{-1}\{e_2\})^T]^T$, and $\{\Gamma\} = [0\ 0\ 0\ ([M]^{-1}\{e_1\})^T]^T$. The 6x6 state matrix $[A]$ is defined as

$$[A] = \begin{bmatrix} [0] & [I] \\ -[M]^{-1}[K] & -[M]^{-1}[C] \end{bmatrix}$$

where [0] is a 3x3 zero matrix and $[I]$ is a 3x3 identity matrix. The friction force, F, was calculated using a sliding mode control algorithm, which is discussed next.

The techniques developed and used in the area of sliding mode control can be used to define the "equivalent dynamics" that exist when sticking takes place. Numerically, sticking is assumed to be possible when $|v_2| \leq 0.001$ m/s. Note that v_2 can be expressed as

$$v_2 = [T]\{y\} \tag{3.5}$$

where $[T] = [0\ 0\ 0\ 0\ 1\ 0]$. During sticking, the slip velocity is identically zero; hence its time derivative must also be zero. Taking the time derivative of (3.5) yields

$$\dot{v}_2 = [T]\{\dot{y}\} = [T]([A]\{y\} + \{B\}F + \{\Gamma\}P) = 0\,. \tag{3.6}$$

Since Equation (3.6) represents the condition when the slip velocity is zero, the friction force, F, must be the force necessary to impose the sticking condition. This force is known as the equivalent friction force, F_{eq}. Solving (3.6) for F yields

$$F_{eq} = -([T]\{B\})^{-1}[T]([A]\{y\} + \{\Gamma\}P)\,. \tag{3.7}$$

Qualitatively, the equivalent friction force is the force necessary to oppose the inertial and external forces to impose the sticking condition. When this force is greater than the maximum allowable friction force, then the system breaks away and starts to slip.

Figure 3.3 shows a flow chart of the logic steps to calculate the friction force. If the slip velocity is equal to or smaller than the Stribeck velocity (v_s = 0.001 m/s), then the equivalent friction force is calculated. However, if this equivalent force is greater than the maximum static friction force (μ*N), then the mass is assumed to break free, and the friction force is set equal to the dynamic friction force given by (3.1) and (3.2).

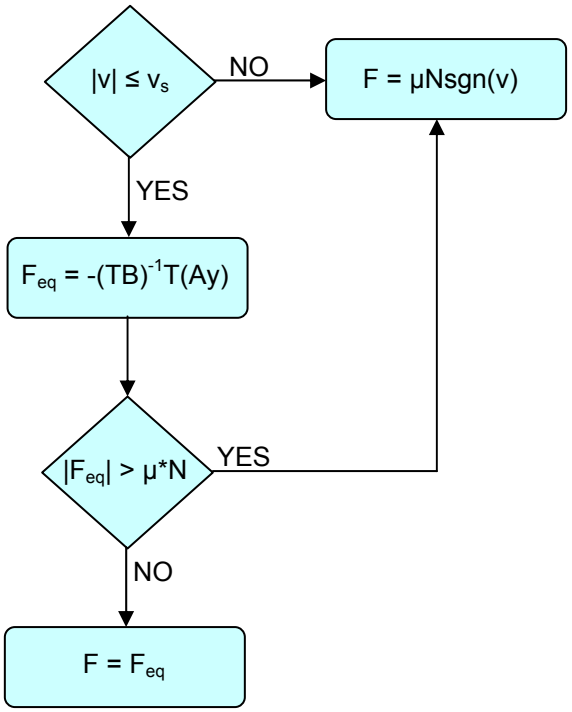

Figure 3.3. Flow chart to calculate friction force (P = 0 case).

To observe the stick-slip behavior of the 2nd mass, the steady-state and free vibration responses of the system were simulated. The goal was to excite the 1st mass to

induce stick-slip motion in the 2nd mass. This stick-slip motion would pump energy from the vibration of the 1st subsystem to the 3rd subsystem.

3.2 System Simulation

Once the equations of motion and the sliding mode control algorithm were established, simulation of the 3DOF system was straight-forward. The method used to simulate the system was the 4th order Runge-Kutta scheme with a fixed time step of 1 ms. Table 3.1 summaries the values used for the simulation.

Table 3.1. Simulation Parameters

System Parameters	Value	Friction Parameters	Value
m_1, m_3	100, 50 kg	μ^*	0.50
m_2	0.25 kg	γ	0.30
k_1, k_4	1000 N/m	β	20.0
k_2, k_3	100 N/m	v_s	0.001 m/s
$\zeta_{1,2,4}$, ζ_3	0.01, 0.05	N	100 N

The 3DOF system can be divided into three subsystems; each subsystem assumes only one of the masses is moving. The natural frequencies for each subsystem are therefore given by

$$\omega_1 = \sqrt{\frac{k_1 + k_2}{m_1}}$$
$$\omega_2 = \sqrt{\frac{k_2 + k_3}{m_2}} \quad . \qquad (3.8abc)$$
$$\omega_3 = \sqrt{\frac{k_3 + k_4}{m_3}}$$

A small amount of viscous damping was added to the system in order to study the interaction of stick-slip energy dissipation and structural damping. The damping coefficients were chosen based on the following relations:

$$\begin{aligned} c_1 &= 2\zeta_1\omega_1 m_1 \\ c_2 &= 2\zeta_2\omega_2 m_2 \\ c_3 &= 2\zeta_3\omega_2 m_3 \\ c_4 &= 2\zeta_4\omega_3 m_4 \end{aligned} \quad . \qquad (3.9abcd)$$

where ζ_i are closely related to the damping ratios of the individual subsystems. The damping ratios are all 1%, except for the 3rd damper, which is 5%. This higher damping ratio for ζ_3 was chosen to ensure adequate excitation of the third subsystem. The partition into three subsystems was useful in analyzing the behavior of the 3DOF system. During periods of sticking by the 2nd mass, the 1st and 3rd masses oscillate like linear single-degree-of-freedom (SDOF) systems with natural frequencies given by ω_1 and ω_3, respectively.

3.3 Steady-State Vibration Response

In order to understand the behavior of the system, the 3DOF system was subjected to harmonic excitation of the form:

$$P(t) = W\sin(\omega_d t) \qquad (3.10)$$

where W is the force amplitude (1500N), ω_d is the driving frequency, and t is the time. Since the stick-slip motion of the 2nd mass exhibits odd numbered harmonics, tuning the 3rd subsystem to one of the harmonics would theoretically produce an internal resonance in the response [39]. The 3rd subsystem was tuned by keeping k_3 and m_3 constant and varying k_4 so that

$$k_4 = \left(\frac{m_3}{m_1}\right) r^2 (k_1 + k_2) - k_3 \tag{3.11}$$

where r is the *tuning ratio* defined as ω_3/ω_1.

Before the steady-state response is presented, it is instructive to examine the linear modes of the 3DOF system in the absence of friction. In particular, the effect of the tuning ratio on the natural frequencies and mode shapes of the system are explored. As seen in Figures 3.4(a) through 3.4(c), mode 1 is mostly dominated by mass 1, mode 2 is dominated by mass 3, and mode 3 is dominated by mass 2. The modes are fairly localized, except when the tuning ratio is 1. At this tuning ratio, mode 1 is a combination of the motion of all three masses. Mode 2 is a symmetric mode where the motion of mass 1 mirrors that of mass 3 while mass 2 is largely immobile. However, mode 3 is seen to be invariant for tuning ratios from 1 to 4.

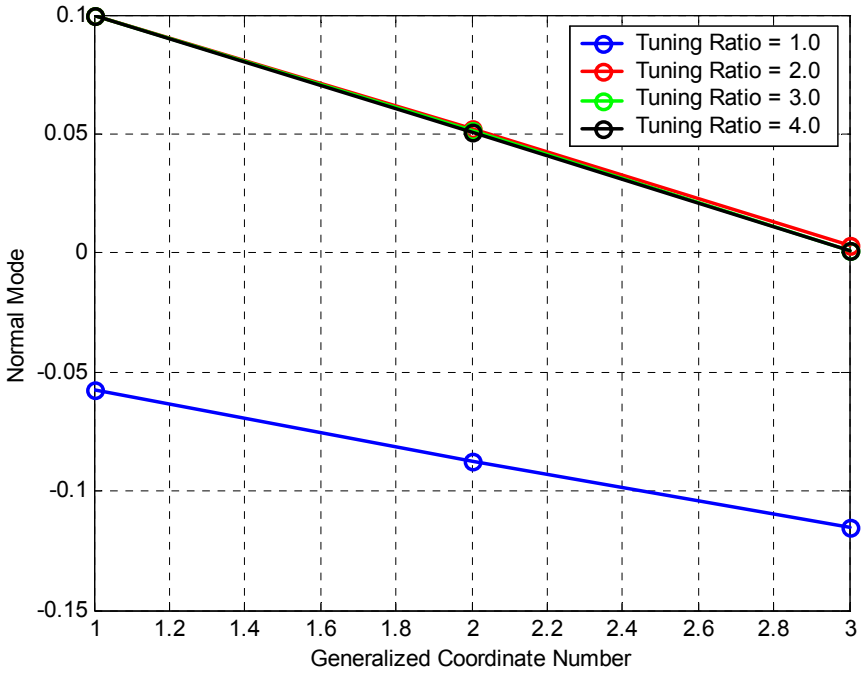
Tuning Ratio = 1.0
Tuning Ratio = 2.0
Tuning Ratio = 3.0
Tuning Ratio = 4.0
Normal Mode
Generalized Coordinate Number
0.1
0.05
0
-0.05
-0.1
-0.15
1
1.2
1.4
1.6
1.8
2
2.2
2.4
2.6
2.8
3

(a)

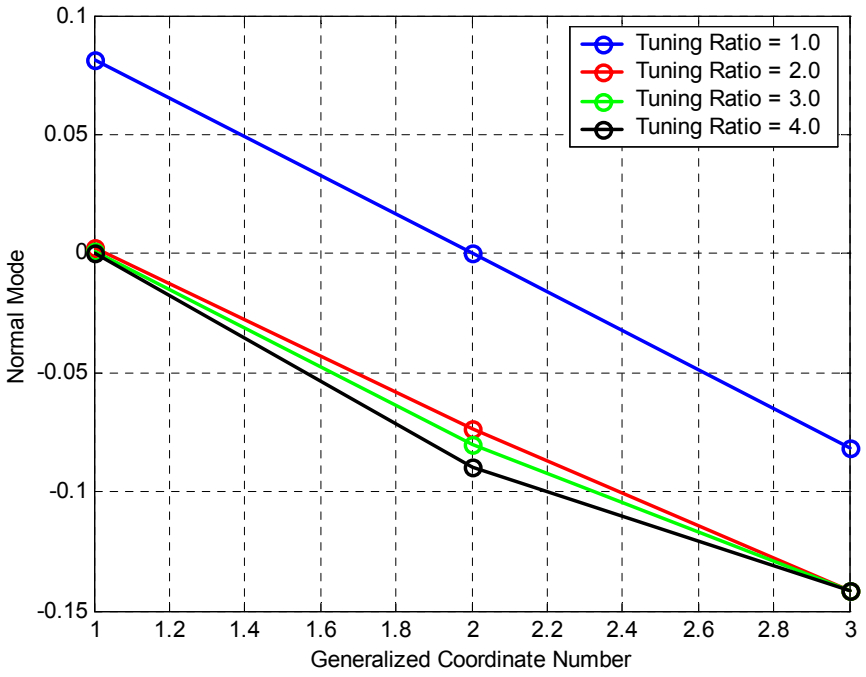
Tuning Ratio = 1.0
Tuning Ratio = 2.0
Tuning Ratio = 3.0
Tuning Ratio = 4.0
Normal Mode
Generalized Coordinate Number
0.1
0.05
0
-0.05
-0.1
-0.15
1
1.2
1.4
1.6
1.8
2
2.2
2.4
2.6
2.8
3

(b)

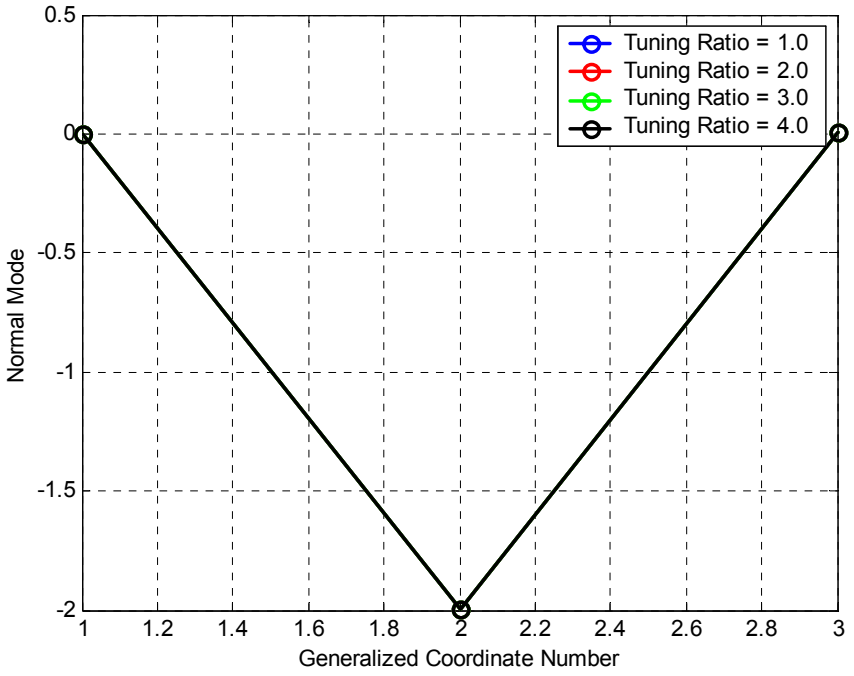

(c)

Figure 3.4. Modal amplitude versus generalized coordinate number for (a) Mode 1, (b) Mode 2, and (c) Mode 3.

The natural frequencies of the linear system follow the same pattern as the mode shapes. At a tuning ratio of 1, modes 1 and 2 have similar natural frequencies. As the tuning ratio is increased from 1, only the natural frequency of mode 2 is increased, whereas the natural frequencies of modes 1 and 3 remain relatively constant. Table 3.2 lists the natural frequencies of the modes for several tuning ratios.

Table 3.2. Natural Frequencies (rad/s)

Tuning Ratio	Mode 1	Mode 2	Mode 3
1.0	3.08	3.32	28.3
2.0	3.24	6.55	28.3
3.0	3.24	9.89	28.3
4.0	3.24	13.2	28.3

The steady-state response of the 3DOF system was obtained by simulating the system until the transient dynamics disappeared. Rather than using the peak displacement per cycle, the amplitude of the steady state response of each mass was described by its root-mean-squared (RMS) displacement:

$$X_{RMS} = \sqrt{\frac{1}{T}\int_{t1}^{t2} x^2 dt} \tag{3.12}$$

where T is some time duration in the steady-state and is given as $T = t_2 - t_1$. The time duration T is defined to be the last 5 periods of the forcing frequency at the end of each simulation. The RMS response was captured over a span of excitation frequency ratios, d, defined as $d = \omega_d/\omega_1$. To expedite the simulations, the end states of each steady-state response were used as the initial conditions for the next frequency ratio. Simulations were always terminated after an integer number of excitation periods had passed.

Figure 3.5 shows the RMS displacements of the 3rd mass as a function of excitation frequency ratio (d) for four tuning ratios, r. This plot shows the presence of internal resonances when the excitation frequency is roughly one-third of the tuned natural frequency of the 3rd subsystem. For example, there is an internal resonance at an excitation ratio of 1.33 when the frequency ratio is 4.0. This phenomenon occurred at all

the tuning ratios except when $r = 3.0$. At this frequency ratio, the internal resonance would occur at $d = 1.0$, which is overshadowed by the resonance of the 1st subsystem. Also noticeable in Figure 3.5 are the internal resonances corresponding to one-fifth of the frequency ratio; e.g., the small peak at $d = 0.6$ when $r = 3$. Lastly, the double peak near $d = 1$ for the case $r = 1$ is due to resonances of the 1st and 2nd modes being closely spaced together.

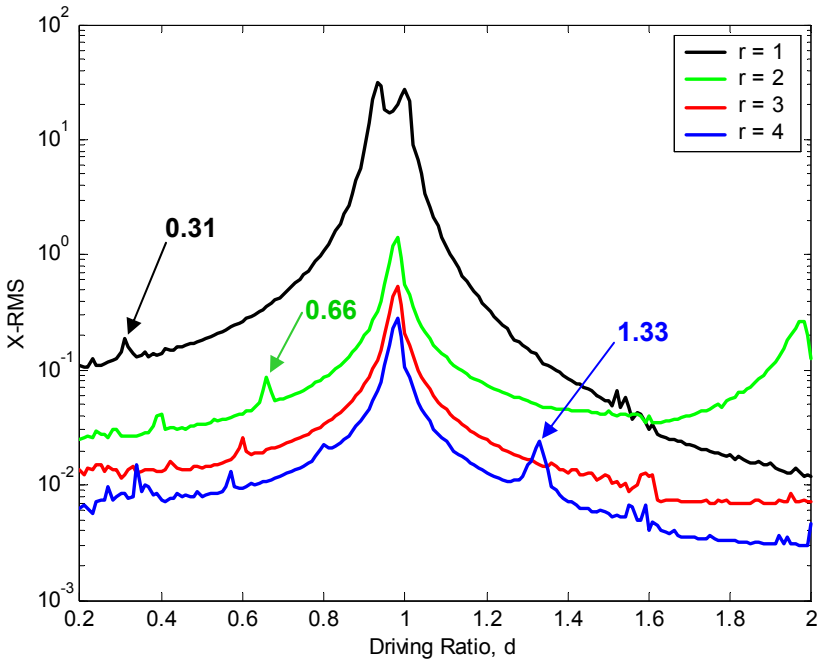

Figure 3.5. RMS displacement of the 3rd mass as a function of excitation frequency ratio.

An examination of the time histories of the steady-state responses revealed a significant amount of stick-slip of the 2nd mass. Thus, excitation at a single frequency is converted into multi-harmonic response by means of the friction nonlinearity. Under favorable tuning conditions, these higher harmonics excite internal resonances as

expected. In the following section, the extent to which subsystem tuning can lead to enhanced energy dissipation during free response is examined.

3.4 Free Vibration Response

The free vibration response of the 3DOF system was simulated to quantify the energy transfer from one subsystem to the other and from low frequencies to higher frequencies. Furthermore, it was important to understand under what states of excitation, friction level, and tuning of the 3rd subsystem did favorable conditions existed for maximum energy dissipation. To simulate the free response, the external force *P(t)* was set to zero and an initial velocity of 2.0 m/s was applied to mass 1.

Figure 3.6 shows a typical free response of the 3-DOF system for a normal force of 40 N and a tuning ratio of r =1. While the displacement and velocity of the 1st mass decrease with approximately linear envelopes of decay, the 2nd mass shows periodic stick-slip behavior until it is completely stuck at a time of about 20 s. This stick-slip behavior is more evident in the velocity of the 2nd mass shown in Figure 3.6(b). The result demonstrates that there is a one-way transfer of vibratory energy from the 1st mass to the 3rd mass because once mass 2 is stuck, masses 1 and 3 oscillate like damped, isolated SDOF systems. Lastly, note that the free response of the 1st mass is similar to having a persistent, nearly harmonic excitation of masses 2 and 3 through the force in spring k_2 and viscous damper c_2.

As shown in Figure 3.6, it is clear that there is a transfer of energy from the 1st mass to the 3rd mass. To quantify how much energy was transferred, it was necessary to look at the energies in the combined system as well as in the individual subsystems. Of

further interest was the energy transfer at frequencies higher than that of the fundamental frequency of the 1st mass. To accomplish this task, the 3rd subsystem was tuned for a range of tuning ratios, *r*. When the stick-slip motion excited a resonance of the 3rd subsystem, there would be a corresponding increase in displacement and velocity. This increased velocity would correlate to higher energy dissipation by the dampers connected to the 3rd mass. Therefore, by examining the energy dissipation in the 3-DOF system, one could quantify the amount of total energy transfer and the energy transfer at higher frequencies.

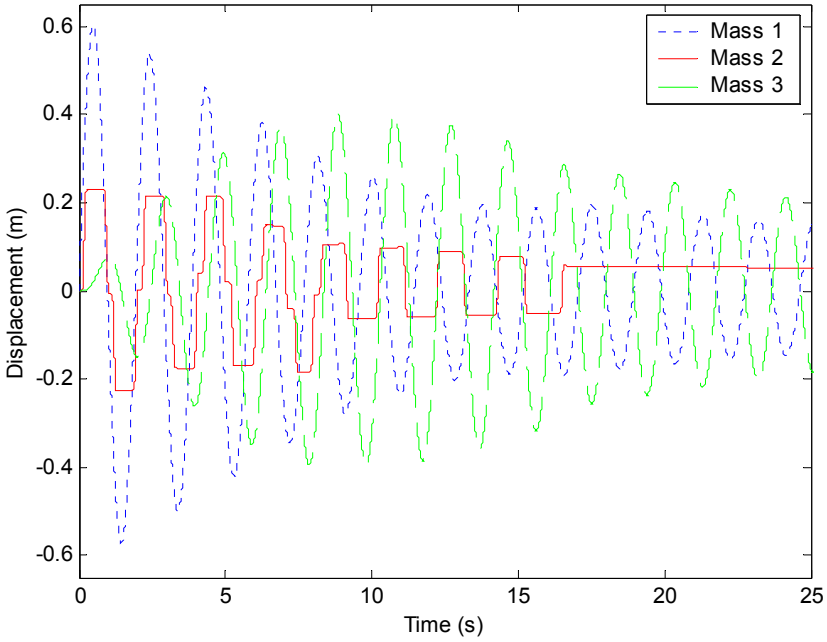

(a)

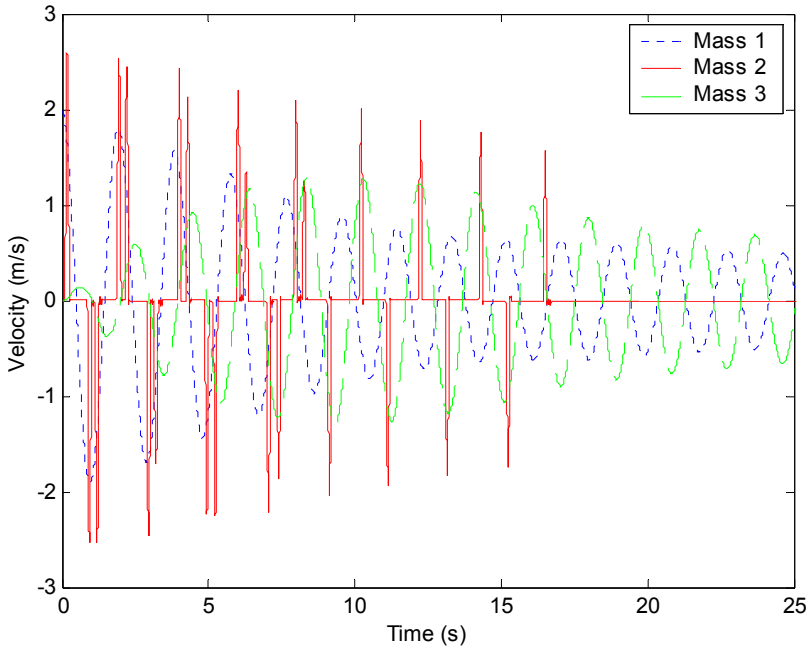

(b)

Figure 3.6. (a) Displacement and (b) velocity time histories of the 3-DOF system (N = 40N, r = 1).

3.5 Energy Dissipation

The total energy, E_{Total}, in the 3DOF system is defined as

$$E_{Total} = \frac{1}{2}\{y\}^T \begin{bmatrix} [K] & [0] \\ [0] & [M] \end{bmatrix} \{y\} \tag{3.13}$$

where $[0]$ is a 3x3 zero matrix. Therefore, the total energy dissipated, E_{dis}, is given by

$$E_{dis} = (E_{Total})_{t=0} - (E_{Total})_{t=tf} \tag{3.14}$$

where tf is the end time of the simulation. The total energy dissipated can be separated into the sum of the energy dissipated by viscous dampers and the energy dissipated by Coulomb friction. If the power dissipated by each viscous damper is denoted as P_i, the total dissipated energy can be expressed as

$$E_{dis} = \sum_{i=1}^{4} \int_{0}^{tf} P_i dt + \left(E_{dis}\right)_{friction} \tag{3.15}$$

where

$$\begin{aligned} P_1 &= c_1 \cdot v_1{}^2 \\ P_2 &= c_2 \left(v_2 - v_1\right)^2 \\ P_3 &= c_3 \left(v_3 - v_2\right)^2 \\ P_4 &= c_4 \cdot v_3{}^2 \end{aligned} \quad . \tag{3.16abcd}$$

By (3.15), it is then possible to indirectly calculate the energy dissipated by friction.

To find the optimal condition for friction to pump energy to higher frequencies, several factors were considered. The total energy of the system was evaluated as a function of the mass ratio (m_3/m_1), the tuning ratio ($r = \omega_3/\omega_1$), the normal force, and the simulation time. A mesh was used to visualize how the total dissipated energy varied as a function of two variables. For the meshes shown in Figures 3.7(a) and 3.7(b), the constant values are the mass ratio (0.5) and the simulation time (15.1 s). This simulation time corresponds to one-half of the time constant of the 1st subsystem, where the time constant = $1/(\omega_1\zeta_1)$. The normal force is varied from 0 to 100 N, in increments of 10 N; and, the tuning ratio is varied from 0.6 to 8.0, in increments of 0.1. Figure 3.7(a) shows the total energy dissipated after 15.1 s of free response. There is a large peak near a tuning ratio of $r = 1$, but there are some smaller peaks as r is increased and N is greater than 80 N. To study this feature more closely, the energy dissipated by the 3rd and 4th dampers over the same time interval are examined, as shown in Figure 3.7(b).

From Figure 3.7(b), there is a large peak in dissipated energy near a tuning ratio of 1. This peak appears to be the result of a "vibration-absorber" effect. As the normal force increases, the absorber effect is less prominent and ripples in the energy dissipation

at higher tuning ratios can be seen. Finally, at $N = 100$ N, there are definite peaks that are evident at certain tuning ratios. The peaks suggest that the force input to mass 3 excites a resonance, thereby causing greater energy dissipation.

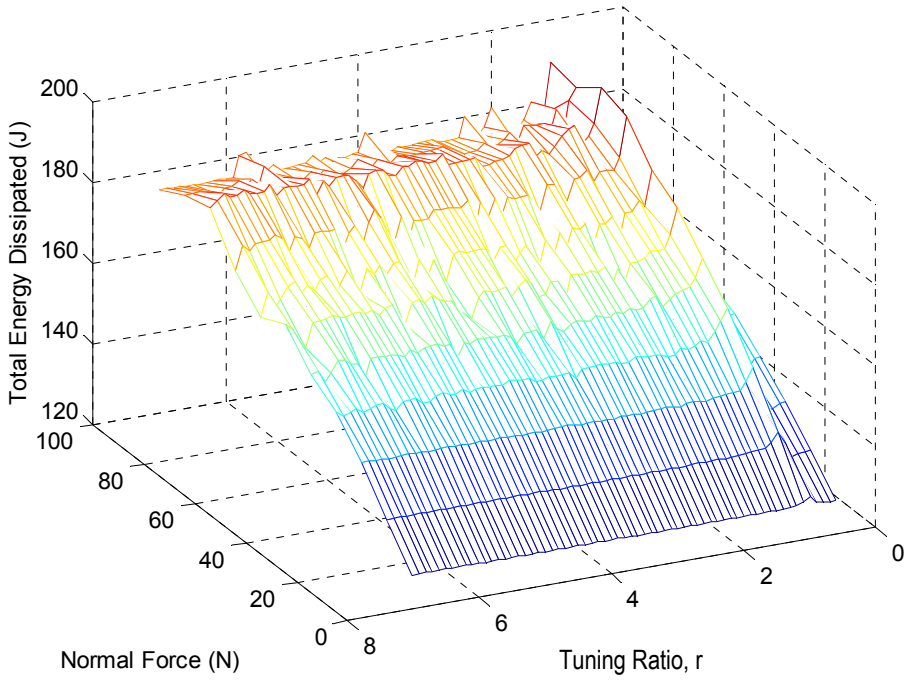

(a)

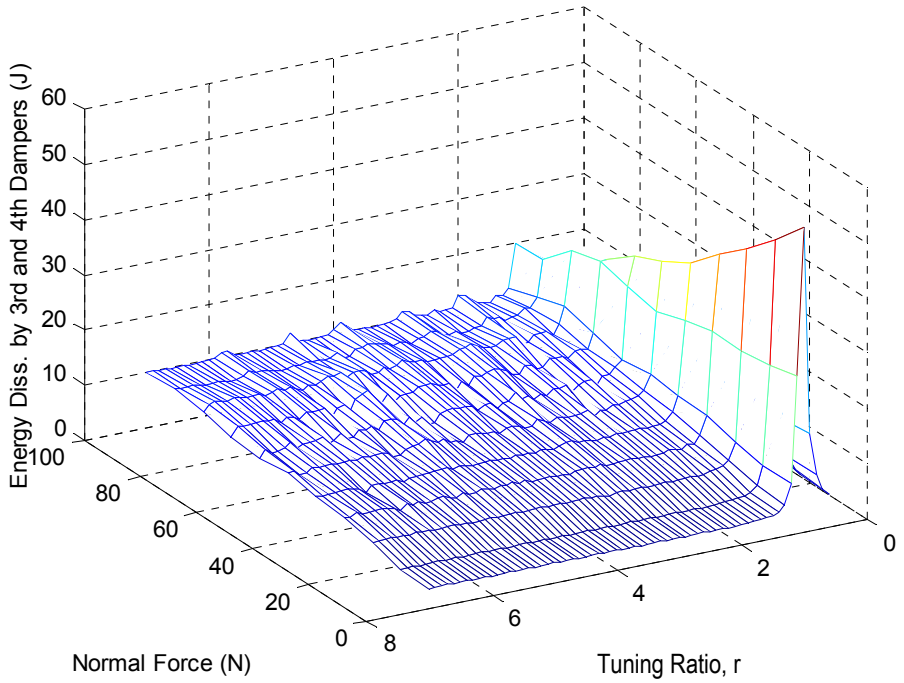

(b)

Figure 3.7. Energy dissipated by the (a) entire system and (b) the 3rd and 4th dampers.

A slice of the mesh in Figure 3.7(b) at $N = 100$ N is shown in Figure 3.8. This plot clearly shows five distinct peaks between the tuning ratios of 2 and 7. These peaks correspond to tuning ratios of r = 2.0, 2.9, 3.9, 4.7, and 5.7. In other words, when tuned to these higher frequencies, the resonance of the 3rd subsystem was excited by the stick-slip motion of the 2nd mass. Therefore, friction on mass 2 pumps energy to higher frequencies. As mentioned previously, the natural frequencies of the 3rd subsystem and that of mode 2 in the linear (frictionless) system are closely related. In fact, the natural frequencies of the 3rd subsystem and that of mode 2 are nearly identical for tuning ratios above 1. Therefore, exciting a resonance of the 3rd subsystem is analogous to exciting the 2nd mode in the linear system.

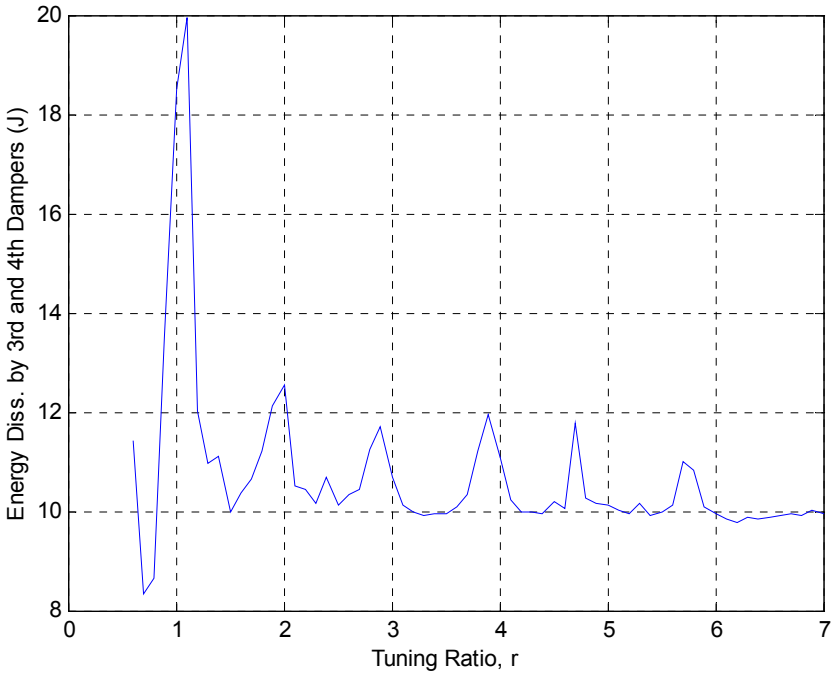

Figure 3.8. Energy dissipated by the 3rd and 4th dampers at $N = 100$ N.

The result shown in Figure 3.8 is interesting because it does not agree with the result from the steady-state response. Although the peaks in Figure 3.8 appear in somewhat regular intervals, they do not occur at only odd harmonics of the frequency of free vibration of the 1st subsystem. This behavior could be attributed to the stick-slip motion during free response (see Figure 5(b)). Since the stick-slip lasts for a finite amount of time, the input into the 3rd subsystem looks like a series of impulses. The impulses have broad frequency content and can excite many frequencies.

To find the best condition for energy dissipation, the energy dissipated by the 3rd and 4th dampers was examined for different levels of normal force and mass ratios (m_3/m_1). Figures 3.9 and 3.10 examine how the energy dissipated by the 3rd and 4th dampers varies with mass ratio and normal force, respectively. Simulation duration times

of longer than 15 s did not have a significant effect on the energy dissipation trends because permanent sticking occurred shortly after 15 s.

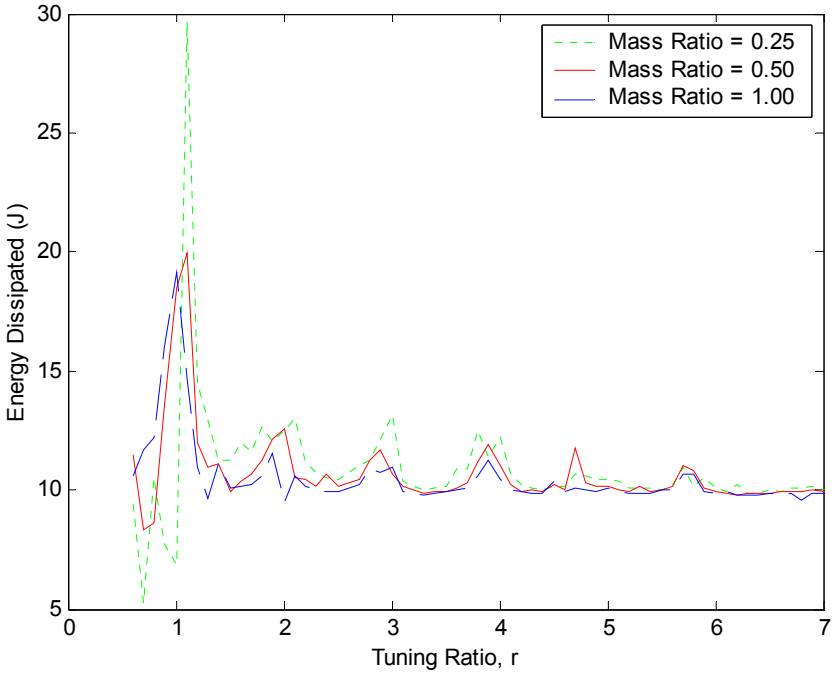

Figure 3.9. Energy dissipated by the 3rd and 4th dampers with varying mass ratios (N = 100 N, t_f = 15.1 s).

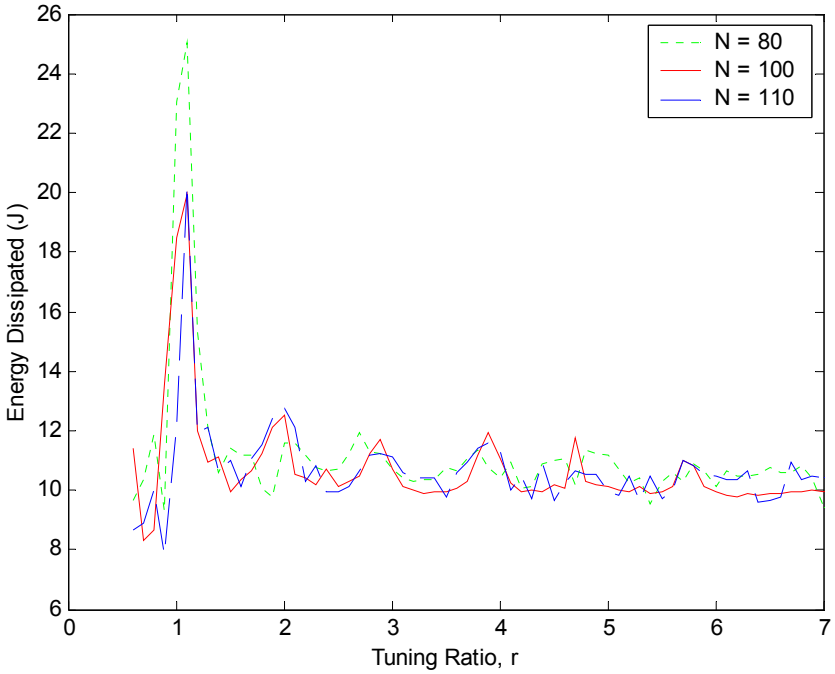

Figure 3.10. Energy dissipated by the 3rd and 4th dampers with varying N (mass ratio = 0.5, t_f = 15.1 s).

Figures 3.9 and 3.10 show that the energy dissipation is sensitive to system parameters. In Figure 3.9, the peaks increase as the 3rd mass decreases. This trend is consistent with a vibration absorber, in which a smaller absorber mass leads to increased absorption over a smaller frequency range. At a mass ratio of 0.25, there is a sharp rise in the 1st peak. However, the 5th and 6th peaks are not as pronounced when compared to a mass ratio of 0.5. Similarly, a mass ratio of 1.0 does not produce noticeable peaks, except when r is near 1.

In Figure 3.10, the peaks at r = 1 decreases as the normal force increases, as mentioned earlier. Similar to the mass ratio, the peaks at tuning ratios larger than 1 are best accentuated at a particular value. In this case, the value is a normal force of 100 N.

At normal forces above 110 N, mass 2 is completely stuck at all times for the initial condition considered here.

The previous results show that friction pumps energy to higher resonances, which serves to increase energy dissipation at the higher resonances. However, it is important to note that the majority of energy dissipation in the 3DOF system is due to friction on mass 2 and the dampers connected to the 1st mass, where the motion originated. For example, at a tuning ratio of 1.1, the energy dissipated by the 3rd and 4th dampers accounts for 11% of the total energy dissipated. At a tuning ratio of 2.0, the energy dissipated by the 3rd and 4th dampers accounts for 7% of the total energy dissipated.

Despite the modest amounts of energy dissipation attributed to the 3rd and 4th dampers, it is necessary to evaluate the advantage of the energy pumping phenomenon versus the case where friction is not present (normal force = 0). To make this comparison, the ratio of the energy dissipated by the 3rd and 4th dampers to the total energy dissipated was evaluated for the friction and non-friction cases. Table 3.3 summarizes the comparison when the normal force is 100 N versus 0 N at tuning ratios corresponding to the peaks in Figure 3.8. For the frictionless case, the energies dissipated are constant after an initial peak at a tuning ratio of 1.

Table 3.3. Percentage of Energy Dissipated by the 3rd and 4th Dampers to the Total Energy Dissipated

Freq. Ratio	**1.1**	**2.0**	**2.9**	**3.9**	**4.7**	**5.7**
N = 100 N	11	7.0	6.7	6.6	6.7	6.1
N = 0 N	42	2.7	2.7	2.7	2.7	2.7

Table 3.3 shows that there is greater dissipation for the friction case except when the tuning ratio is at 1.1. Although the advantage is small (about 4% of the total energy dissipated), this result demonstrates that the pumping of energy to higher resonances can serve as a tool for increased dissipation. As for the case where the tuning ratio is 1.1, there is greater dissipation by the 3rd and 4th dampers of the frictionless system; however, the total energy dissipation is greater in the system with friction. At this tuning ratio, the total energy dissipated by the frictionless system is 130.4 J, versus 189.7 J for the system with friction.

This investigation was admittedly simple in order to permit a more thorough understanding of the phenomenon. Specifically, the joint model was represented by simple SDOF subsystems. The next chapter applies the Stribeck friction model to a more complicated joint model. It is expected that the results seen in this study can be extended to higher order systems.

CHAPTER 4

ENERGY TRANSFER AND DISSIPATION: CONTINUOUS SYSTEM

Up to this point, the focus has been on the effects of friction in discrete systems. Because of the relative simplicity of the discrete systems, it is possible to thoroughly examine and understand the behavior and features of the frictional interface. Results from Chapter 3 suggest that a frictional interface can pump vibratory motion from one frequency to higher frequencies, thus exciting higher resonances. This chapter applies the concepts learned in Chapter 3 to a more complicated, and realistic, joint configuration. Similar to the analysis of the 3DOF system, the energy transfer and dissipation between subsystems connected by a frictional interface is explored in this chapter. In particular, the relationship between the tuning parameter and energy dissipation is examined.

Presented first is the model of the continuous beam system and the governing equations of motion. The beam dynamics are approximated using a finite modal (Ritz) series. Next, a state-space model is developed to simulate the response of the system. Following the development of the state-space model is an evaluation of the forced steady-state response of the beam alone, as well as the entire system. Afterwards, the energy transfer and dissipation between the subsystems during free response, as well as the controllability of the entire system are discussed. Finally, this chapter concludes with the sensitivity of the system to tuning parameters and friction laws.

4.1 System Model

An improvement to the 3DOF joint model in Chapter 3 is shown in Figure 4.1. The jointed structure is represented by a cantilever beam connected to a SDOF spring-mass-damper system via a friction damper attachment. An advantage of this model over the 3DOF system is the "floating" joint configuration. This configuration means that the coupling between the two structures is through the frictional element itself. In contrast to the 3DOF system of Chapter 3, the two subsystems of the beam-mass system continue to interact, even when the interface is fully stuck. This configuration is more realistic for many types of structural connectors. Another advantage of this model is that, theoretically, the beam has an infinite amount of modes. Although a finite number of modes will be used in this study, the multi-mode property of the beam creates more complex interactions between the beam and the attached SDOF system.

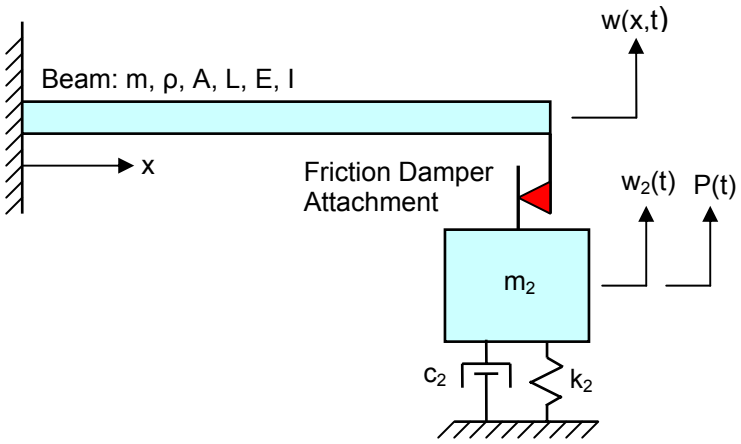

Figure 4.1. Beam-mass system model of a jointed structure.

The beam properties m, ρ, A, L, E, and I represent the mass, density, cross-sectional area, Young's Modulus, and moment of inertia, respectively. The parameter x

denotes the displacement along the beam, with $x = 0$ defined as the clamped end and $x = L$ is at the friction attachment. Transverse displacement of the beam, $w(x,t)$, is a function of the spatial coordinate and time, t. For the attached SDOF system, the mass is m_2, the spring constant is k_2, the damper constant is c_2, and $w_2(t)$ is the displacement. The function, $P(t)$, represents an external force applied directly to mass 2.

The friction attachment can be modeled as a pair of equal and opposite friction forces acting on the end of the beam and on mass 2. This friction force would be dependent on the relative velocity between mass 2 and the velocity at the end of the beam, defined as $v_{rel} = \dot{w}_2(t) - \dot{w}(L,t)$. Therefore, the friction force, $F(v)$, is given by

$$F(v) = \mu N \operatorname{sgn}(v_{rel}) \tag{4.1}$$

where N is the normal force and μ is the Stribeck friction coefficient given by Equation (3.2). As in Chapter 3, the coefficient α in Equation (3.2) is set to zero in this case as well. Furthermore, parameters for the friction model can be found in Table 3.1.

4.1.1 Governing Equations

The governing equations of motion for the system shown in Figure 4.1 can be broken into two sets: a set of equations for the beam and a set for the attached SDOF system. For an unforced, uniform beam, the partial differential equation describing the flexural displacement is based on the Bernoulli-Euler model and is given by

$$EI \frac{\partial^4 w(x,t)}{\partial x^4} + \rho A \ddot{w}(x,t) = 0 \tag{4.2}$$

where ∂^n represents an n[th] order partial derivative and the overdot represents a partial derivative with respect to time. The equation for the SDOF system is much simpler and is given by

$$m_2\ddot{w}_2(t) + c_2\dot{w}_2(t) + k_2 w_2(t) = P(t) - F(v)\,. \tag{4.3}$$

The sign of the friction force in (4.3) is determined by examining a free body diagram of the system. Since v_{rel} is defined as the velocity of the mass minus the velocity at the end of the beam, the friction force must oppose the motion of the mass when v_{rel} is positive. At the end of the beam, this friction force acts in a positive (up) direction when v_{rel} is positive.

The solution to (4.2) can be approximated by a finite modal Ritz series

$$w(x,t) = \sum_{i=1}^{NM} z_i(t)\varphi_i(x) \tag{4.4}$$

where $z_i(t)$ is the normal mode amplitude of the i[th] mode, $\varphi_i(x)$, and NM is the number of modes. For a uniform cantilever beam, the normal mode is given by

$$\varphi_i(x) = \frac{1}{\sqrt{mL}}\left\{\cosh\frac{\lambda_i x}{L} - \cos\frac{\lambda_i x}{L} - \left(\frac{\cosh\lambda_i + \cos\lambda_i}{\sinh\lambda_i + \sin\lambda_i}\right)\left(\sinh\frac{\lambda_i x}{L} - \sin\frac{\lambda_i x}{L}\right)\right\} \tag{4.5}$$

where λ_i is the i[th] root of the characteristic equation

$$\cosh\lambda_i \cos\lambda_i + 1 = 0\,. \tag{4.6}$$

The first two nonzero roots of (4.6) can be found numerically and they are $\lambda_1 = 1.8751$ and $\lambda_2 = 4.6941$. For $i \geq 3$, the root can be approximated by the asymptotic relationship

$$\lambda_i \approx \frac{2i-1}{2}\pi\,. \tag{4.7}$$

From the roots of the characteristic equation, the i[th] natural frequency of the beam, ω_i, is given by

$$\omega_i = \left(\frac{EI}{\rho A L^4} \right)^{1/2} \lambda_i^2 . \tag{4.8}$$

The normal mode amplitudes, z_i, are governed by a set of 2nd order differential equations

$$\ddot{z}_i + 2\zeta_i \omega_i \dot{z}_i + \omega_i^2 z_i = F(v)\varphi_i(L) \tag{4.9}$$

where ζ_i is the damping ratio for the ith mode. Using orthogonality, it can be shown that the mode function, φ_i, is normalized such that the modal masses are unity. For a more thorough discussion of the equations of motion for a continuous beam, see References [20] and [40].

4.1.2 System Properties

The properties for the beam system are given in Table 4.1. With the exception of the normal force, the values for the Stribeck friction model are the same as those used in the 3DOF system (see Table 3.1). The modal damping ratio, ζ_i, is constant for all modes. As a note, the mass of the beam can be calculated by $m = \rho AL = 0.636$ kg; and, the damper constant is calculated by $c_2 = 2\xi_2 \sqrt{k_2 m_2}$, where ξ_2 is the prescribed damping ratio of the uncoupled mass-spring-damper system.

Table 4.1. Properties for the Beam-Mass System

Beam Properties	Value	Other	Value
ρA	0.636 kg/m	m_2	1.0 kg
L	1.0 m	k_2	400 N/m
E	7.3×10^{10} N/m^2	ζ_2	0.01
I	1.325×10^{-10} m^4	N	5 N
ζ_i	0.01		

To better understand the beam system, it is useful to study the linear modes of each subsystem without the friction attachment. For the spring-mass subsystem, the undamped natural frequency, ω_{n2}, is simply given by

$$\omega_{n2} = \sqrt{\frac{k_2}{m_2}}. \tag{4.10}$$

Later in this chapter, this frequency, also known as the tuning frequency, will be varied to study the energy dissipation in the entire system. For the beam, the undamped natural frequencies and mode shapes can be calculated using (4.8) and (4.5), respectively. Figure 4.2 shows the normalized mode shapes and natural frequencies for the first four modes of the beam.

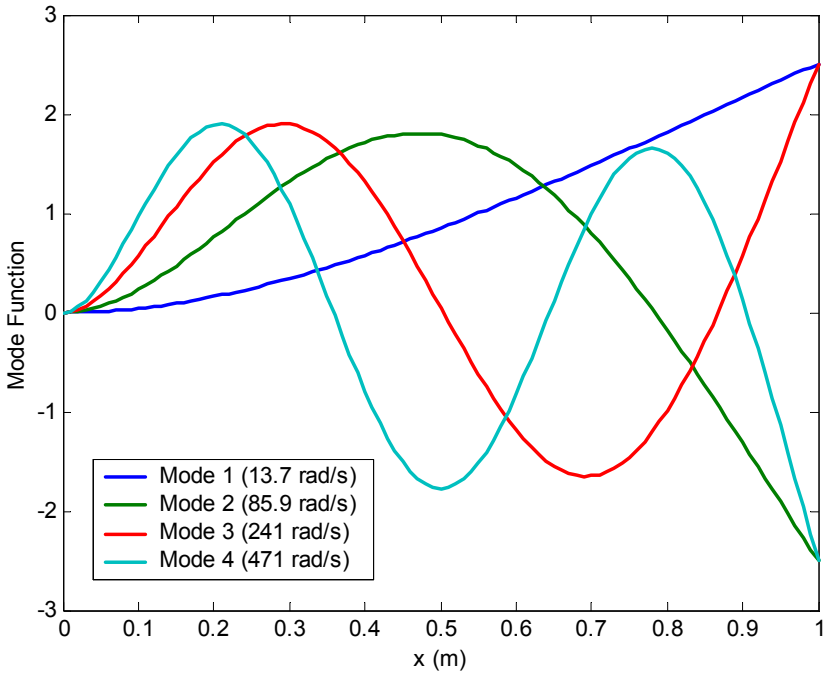

Figure 4.2. Mode function and natural frequencies for the cantilever beam.

4.1.3 State-Space Formulation

Once the governing equations and properties for the beam system are established, a state-space formulation is used to simulate the system. The state-space contains both the modal coordinates, z_i, and the position coordinate of the attached mass, $w_2(t)$. Furthermore, the state vector contains the 1st time derivative of these coordinates as well. Therefore, the dimension of the state-space is $2NM + 2$ and the state vector, $\{q\}$, is defined as

$$\{q\} = [z_1 \; z_2 \ldots \; z_{NM} \; \dot{z}_1 \; \dot{z}_2 \ldots \; \dot{z}_{NM} \; w_2 \; \dot{w}_2]^T . \tag{4.11}$$

With the state vector defined, the first-order, state-space equation can be expressed as

$$\{\dot{q}\} = [A]\{q\} + \{B\}F + \{\Gamma\}P \tag{4.12}$$

where $[A]$ is the state matrix with dimension $2NM + 2$, $\{B\}$ is the state input vector associated with the friction force, and $\{\Gamma\}$ is the state input vector associated with the external force. Notice that this equation is consistent with the form in (3.4) in Chapter 3; however, the variables are different in this case.

The state matrix, $[A]$, and state input vector, $[B]$, can be divided into sub-matrices and sub-vectors as follows

$$[A] = \begin{bmatrix} [A_B] & [0] \\ [0] & [A_M] \end{bmatrix}, \ \{B\} = \begin{Bmatrix} \{B_B\} \\ \{B_M\} \end{Bmatrix} \tag{4.13}$$

where $[A_B]$ and $[A_M]$ are the state matrices for the beam and mass, respectively; and, $\{B_B\}$ and $\{B_M\}$ are the state input vectors for the beam and mass, respectively. Correspondingly, the dimensions for $[A_B]$ and $\{B_B\}$ are $2NM$. For $[A_M]$ and $\{B_M\}$, the dimension is 2. Lastly, the vector $\{\Gamma\}$ is given by

$$\{\Gamma\} = [0 \ldots 0 \ \ 1/m_2]^T . \tag{4.14}$$

The state matrix $[A_B]$ can be further broken into diagonalized stiffness and damping matrices as follows

$$[A_B] = \begin{bmatrix} [0] & [I] \\ -[\widetilde{K}] & -[\widetilde{C}] \end{bmatrix}, \tag{4.15}$$

where

$$[\widetilde{K}] = \begin{bmatrix} \omega_1^2 & 0 & \cdots & 0 \\ 0 & \omega_2^2 & \cdots & 0 \\ \vdots & \vdots & \ddots & \vdots \\ 0 & 0 & \cdots & \omega_{NM}^2 \end{bmatrix}, \ [\widetilde{C}] = \begin{bmatrix} 2\zeta_1\omega_1 & 0 & \cdots & 0 \\ 0 & 2\zeta_2\omega_2 & \cdots & 0 \\ \vdots & \vdots & \ddots & \vdots \\ 0 & 0 & \cdots & 2\zeta_{NM}\omega_{NM} \end{bmatrix}, \tag{4.16}$$

and $[I]$ is the identity matrix. The dimension of the all the sub-matrices in (4.15) is NM. The state input vector $\{B_B\}$ is given by

$$\{B_B\} = [0 \ \ldots \ 0 \quad \varphi_1(L) \ \varphi_2(L) \ldots \ \varphi_{NM}(L)]^T . \tag{4.17}$$

Finally, the state matrix, $[A_M]$, and state input vector, $\{B_M\}$, are defined as

$$[A_M] = \begin{bmatrix} 0 & 1 \\ -k_2/m_2 & -c_2/m_2 \end{bmatrix}, \ \{B_M\} = -\begin{Bmatrix} 0 \\ 1/m_2 \end{Bmatrix}. \tag{4.18}$$

Since the state vector contains the modal coordinates, Equation (4.4) must be used to calculate the displacement of the beam. To calculate the velocity of the beam, (4.4) is differentiated with respect to time so that

$$\dot{w}(x,t) = \sum_{i=1}^{NM} \dot{z}_i(t)\varphi_i(x). \tag{4.19}$$

To calculate the friction force, the same switching algorithm used in Chapter 3 is used here (see Section 3.1). Following the steps outlined in Section 3.1, the relative velocity is given by

$$v_{rel} = \dot{w}_2(t) - \dot{w}(L,t) = \dot{w}_2(t) - \sum_{i=1}^{NM} \dot{z}_i(t)\varphi_i(L) = [T]\{q\} \tag{4.20}$$

where

$$[T] = [0 \ \ldots \ 0 \quad -\varphi_1(L) \ -\varphi_2(L) \ \ldots \ -\varphi_{NM}(L) \ 0 \ 1]. \tag{4.21}$$

Similarly, the equivalent friction force, F_{eq}, in this case is

$$F_{eq} = -\left([T]\{B\}\right)^{-1}[T]\left([A]\{y\} + \{\Gamma\}P\right). \tag{4.22}$$

4.2 System Simulation

Initial simulation of the system of equations given by (4.12) was performed using the 4th order Runge-Kutta method with a fixed time step of $5\text{x}10^{-4}$ s. Not only does the accuracy of the solution hinge on the size of the time step, it also depends on the number

of modes, *NM*, used in the modal series. Theoretically, the approximate solution given by (4.4) approaches the true solution as *NM* approaches infinity.

4.2.1 Mode Number Convergence

A study was conducted to find out how many modes were necessary for the response of the beam to converge. Since the friction attachment is at the end of the beam, it was expected that the motion of the beam would be dominated by the first few modes. Figures 4.3(a) and 4.3(b) plots the response at $x = L$ for several cases with different values of *NM*. The excitation was an initial velocity of 2.0 m/s applied onto the attached mass.

From the figures below, the responses using 2 modes is not accurate compared to the responses with 4 or 8 modes. However, the response using 4 modes accurately captures the response and there is little difference between using 4 modes and using 8 modes. Therefore, for the remainder of the studies in this Chapter, 4 modes are used to describe the beam dynamics.

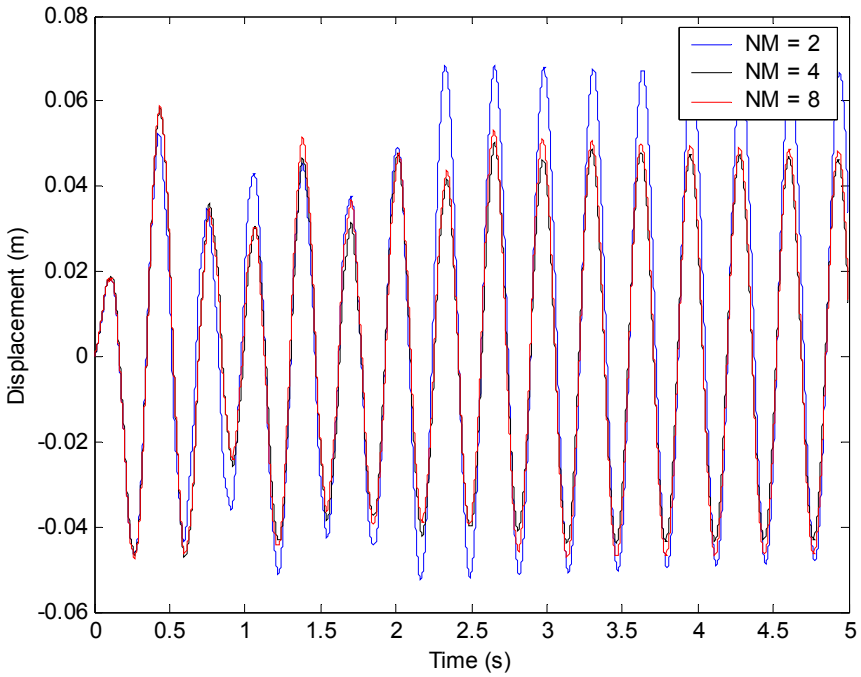

(a)

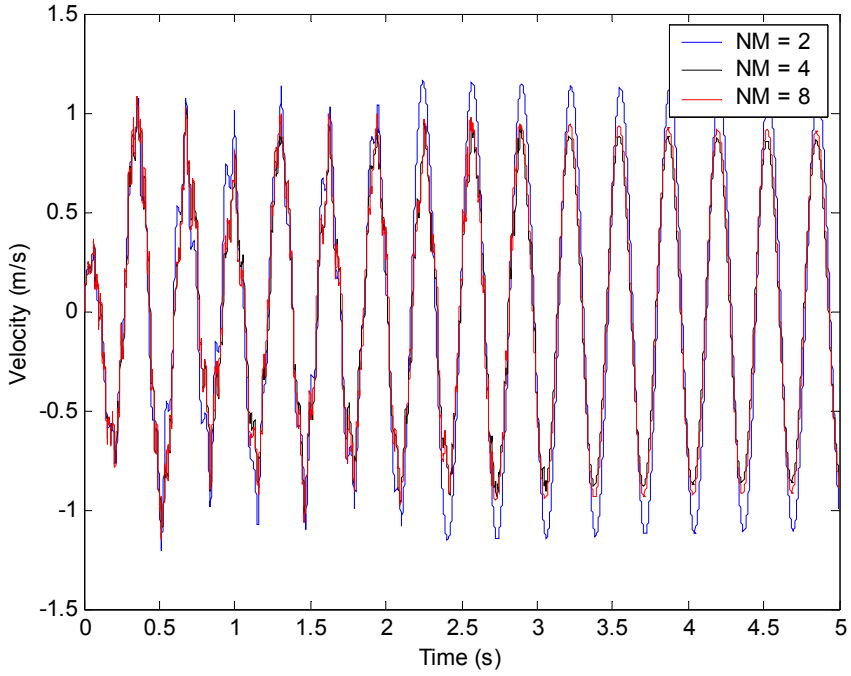

(b)

Figure 4.3. (a) Displacement and (b) velocity response at $x = L$ on the beam.

4.2.2 Steady-State Frequency Response

To gain insights into the beam system, the steady-state forced response was studied. First, the steady-state response of the beam without any attachments was examined. In this case, the forcing function, *P(t)*, is applied at the end of the beam and is given by

$$P(t) = W \sin(\omega_d t) \tag{4.23}$$

where W is the amplitude of the force and ω_d is the driving frequency. Figure 4.4 shows the displacement magnitude of the frequency response function at the end of the beam ($x = L$) for a driving frequency range of 5 to 100 rad/s. This range was selected because it captured the first two modes of the beam, which is the focus of further investigation in this chapter. From Figure 4.4, the 1st and 2nd modes of the beam at 13.7 and 85.9 rad/s, respectively, can be easily seen, as well as what appears to be a zero at 60.3 rad/s. In Figure 4.5, the phase angle of the response is shown. From this plot, the zero at 60.3 rad/s is confirmed because of the 180 degree phase shift near this frequency.

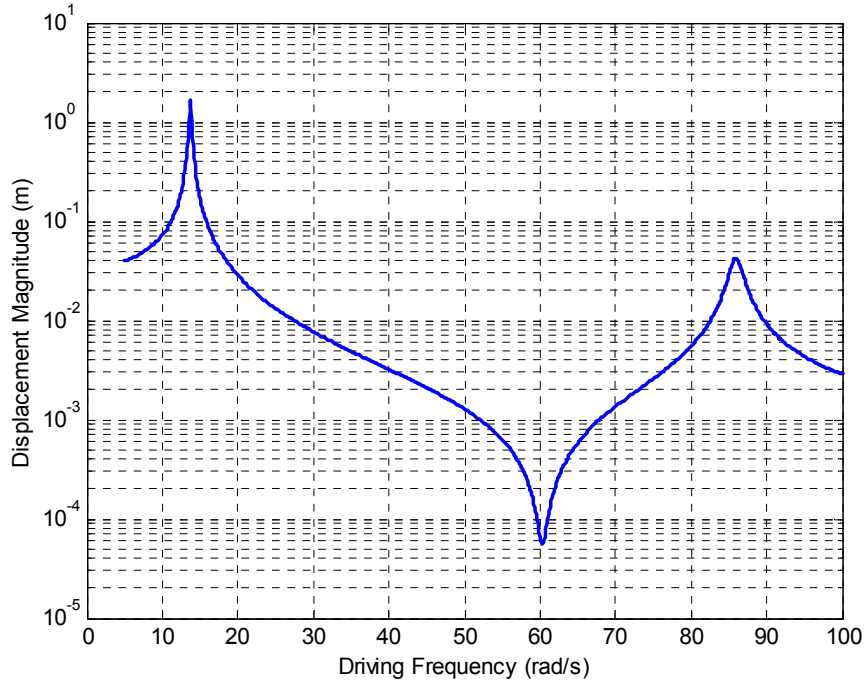

Figure 4.4. Magnitude of the frequency response of the beam at $x = L$.

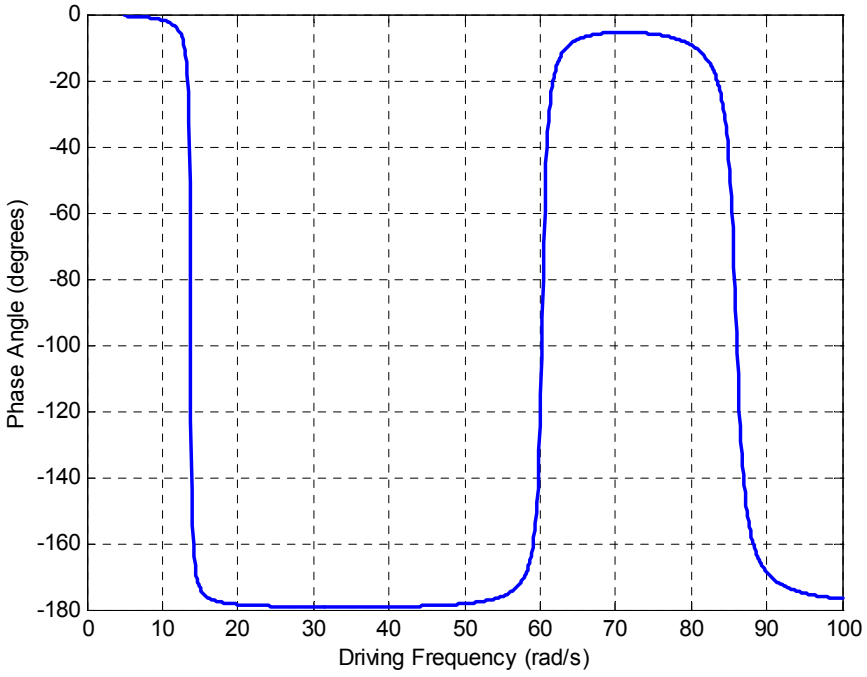

Figure 4.5. Phase angle of the response of the beam at $x = L$.

Once the steady-state response of the beam was characterized, the frequency response of entire beam system was evaluated. The forcing function given by (4.23) is now applied to the attached mass, as seen in Figure 4.1. Again, the response was evaluated at the end of the beam, where the friction damper is attached. For the case shown in Figures 4.6 and 4.7, the natural frequency of the attached SDOF system, ω_{n2}, was tuned to 50 rad/s so that it was well separated from the modes of the beam. Like the 3DOF system, tuning was accomplished by keeping the mass of the SDOF system, m_2, constant while changing k_2 such that

$$k_2 = m_2 \omega_{n2}^2 . \tag{4.24}$$

This tuning parameter will be of greater importance in the next section.

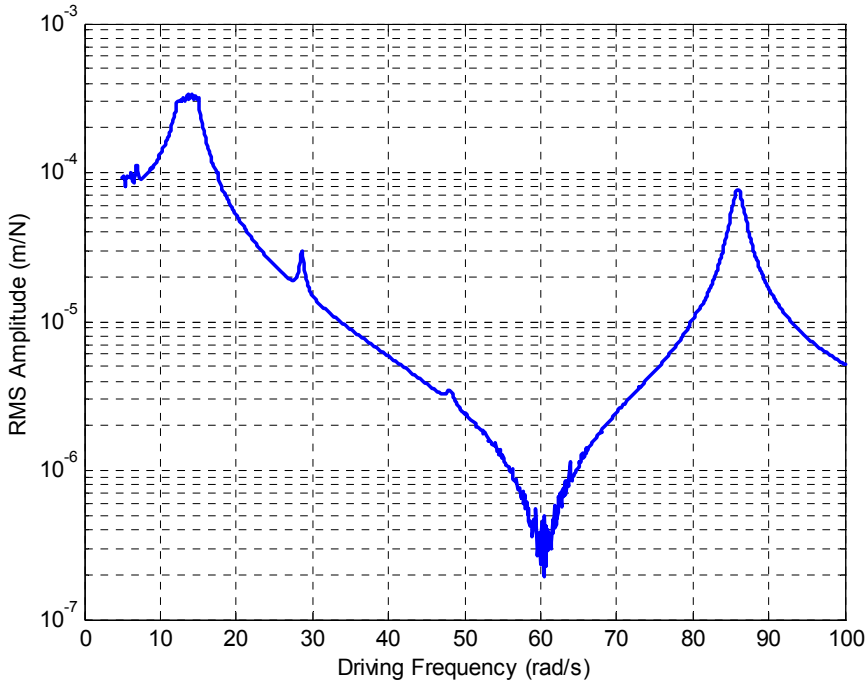

Figure 4.6. RMS Displacement frequency response of the beam system at $x = L$.

There are several interesting features about the frequency response of the beam in Figure 4.6. The first feature is the noisy areas of the plot, especially around the null in the vicinity of 60.3 rad/s. This problem can be attributed to a relative lack of precision in the switching algorithm caused by a coarse time step. The noisy areas diminish as the time step is reduced. Secondly, there is a flat top in the response in the region of the 1st mode of the beam (13.7 rad/s). This is caused by a variation in the resonant frequency as different levels of slip occur. If the interface is almost stuck, the beam-mass system will exhibit a resonance at a frequency somewhat lower than the first beam natural frequency. However, if excited at that resonance, the interface will break free, thereby adding damping while disrupting the resonance. This phenomenon creates a saturation-like appearance in this region. Lastly, the most important effect is the presence of internal resonances in the frequency response. In Figure 4.6, there is an internal resonance at 28.6 rad/s, corresponding to 1/3 of the frequency of the 2nd mode of the beam (85.9 rad/s). Also noticeable is a small internal resonance peak at 48.1 rad/s, or 1/5 of the frequency of the 3rd mode of the beam (241 rad/s). The presence of the internal resonances is much more evident in the modal response of the beam. Figure 4.7 shows the frequency response of the decoupled modal coordinates, z_i, of the beam. Aside from the noisy region around the 1st mode of the beam, the presence of internal resonances for each mode is clear. Each peak corresponds to an odd harmonic of the natural frequency of the particular mode, for example 1/3, 1/5, 1/7, etc.

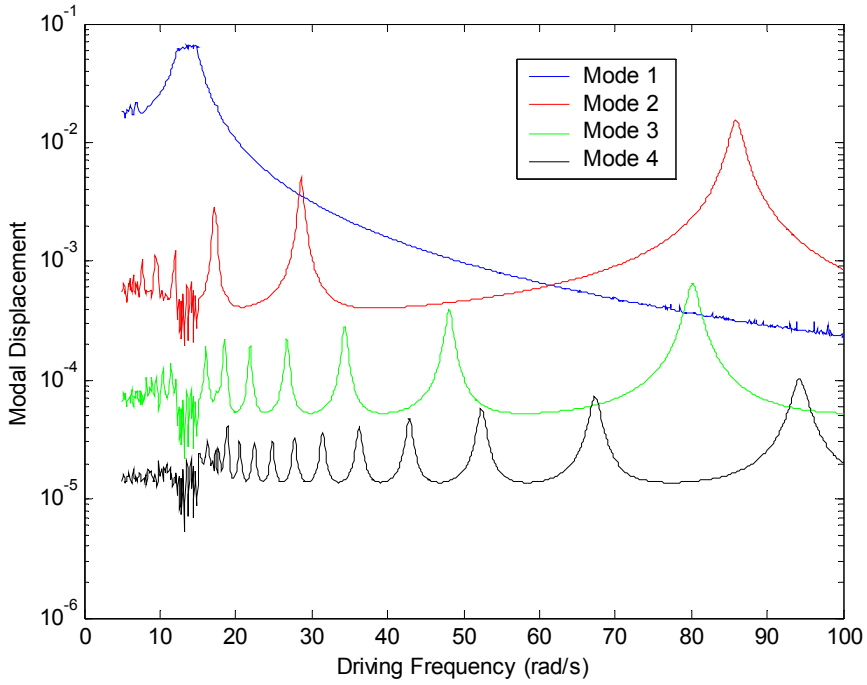

Figure 4.7. Modal displacement response of the beam system.

The apprearance of internal resonances suggest that the friction damper in the beam-mass system pumps energy to higher modes, i.e., the friction nonlinearity converts excitation at one frequency into a multi-harmonic excitation. The next section examines how tuning the SDOF system to the internal resonances can affect the energy dissipation in the free response of the system.

4.3 Energy Dissipation

The energy dissipation of the beam-mass system was evaluated by observing the free response of the system. Excitation to the system was an initial velocity of 2.0 m/s applied onto the attached mass while the external force, *P(t)*, was set to zero. To isolate the energy dissipation to the beam and the friction damper, the viscous damper attached

to the mass, c_2, was set to zero as well. Lastly, the energy dissipated was evaluated after a time, *tf*, equal to 10 natural periods of the 1st mode of the beam. This time is approximately 4.6 s.

4.3.1 System Energies

The energy dissipated in the system can be calculated by taking the initial system energy minus the system energy after *tf* seconds. Since the excitation is an initial velocity, the initial system energy, $(E_{Total})_{t=0}$, is therefore

$$\left(E_{Total}\right)_{t=0} = \frac{1}{2} m_2 \dot{w}_2^2 (t=0) \tag{4.25}$$

where $\dot{w}_2(t=0)$ is the initial velocity. At any other time, the total energy in the system is the sum of the beam energy, $E_{beam,}$ and the energy of the attached mass system, E_{mass}. The beam and mass energies are composed of the kinetic and potential energies as follows:

$$E_{beam} = \frac{1}{2}\sum_{i=1}^{NM} \dot{z}_i^2 + \frac{1}{2}\sum_{i=1}^{NM} \omega_i^2 z_i^2 \tag{4.26}$$

$$E_{mass} = \frac{1}{2} m_2 \dot{w}_2^2 + \frac{1}{2} k_2 w_2^2 . \tag{4.27}$$

Therefore, the total dissipated energy after *tf* seconds is given by

$$E_{dis} = (E_{Total})_{t=0} - (E_{beam} + E_{mass})_{t=tf} . \tag{4.28}$$

The energy dissipated in the system was evaluated as a function of the tuning frequency, or ω_{n2}. Similar to the analysis of the 3DOF system in Chapter 3, the purpose of varying the tuning frequency was to determine favorable tuning conditions to maximize energy dissipation in the system. In particular, at what values of tuning

frequency and normal force would there exist a "sweet spot" where the energy dissipation is maximum? Intuitively, this sweet spot should occur when the tuning frequency is at an internal resonance of the system. If the tuning frequency is near a resonance of the beam, then the relative motion between the beam and mass would be small, thus causing the friction damper to be stuck. In this case, the majority of energy dissipation will be through the modal damping of the beam. Conversely, if the tuning frequency is far from a beam resonance, significant sliding should occur between the beam and the mass and energy dissipation would be primarily due to friction. However, if the tuning frequency is equal to that of an internal resonance, then both the modal damping in the beam and the friction would contribute to the energy dissipation. In this scenario, energy would be pumped to a higher mode in the beam, thus causing the energy to be dissipated faster. Also, since the beam is vibrating at an odd harmonic above the frequency of the mass, the motion between the two systems should be out of phase. This motion should induce slip in the friction damper, thus dissipating energy.

To explore the effects of tuning, the energy in the system was evaluated as a function of the tuning frequency and the normal force at the friction damper. Figure 4.8 shows a mesh of the total energy *remaining* after 4.6 s of free response. This parameter was chosen because it was easier to visualize than a mesh of the total energy dissipated. For the mesh shown in Figure 4.8, the high values indicate poor energy dissipation while low values signal good energy dissipation. The range for the tuning frequency and normal force are 5 to 100 rad/s and 1 to 10 N, respectively.

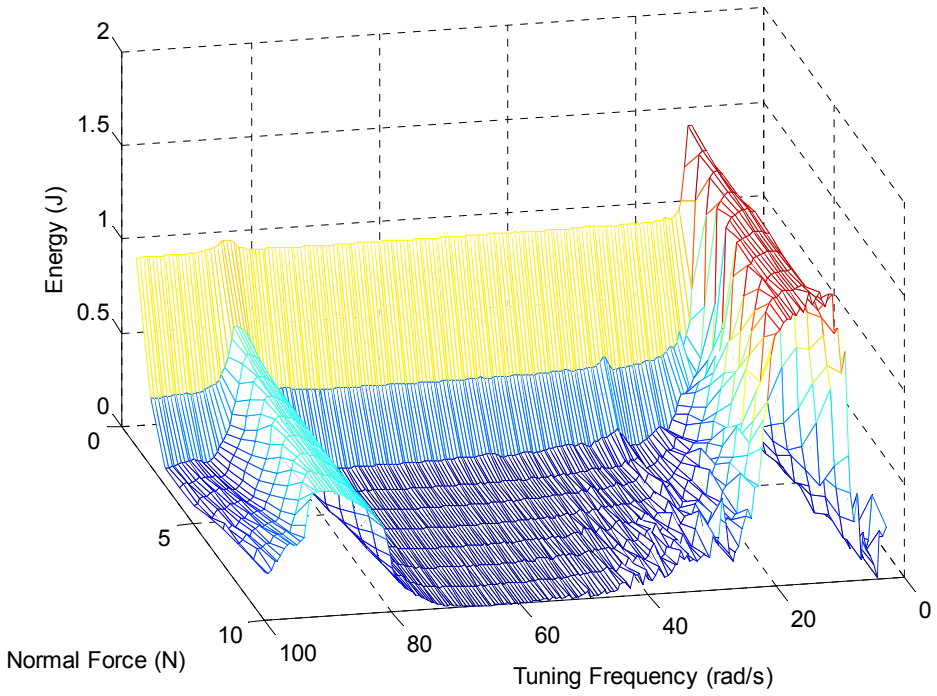

Figure 4.8. Total system energy after 4.6s of free response.

From Figure 4.8, it is clear that the poorest energy dissipation occurs when the tuning frequency is near natural frequencies of the beam modes. However, a surprising result is that the energy dissipation when the tuning frequency is at an internal resonance (28.6 rad/s) is worse than the energy dissipation when the system is completely mistuned. There are peaks in the energy at the internal resonance, especially as the normal force increases. On the other hand, the area around 60 rad/s stays relatively flat above $N = 2$ and is the lowest point in the mesh.

The results suggest that friction plays the dominant role in dissipating energy in the system. From Figure 4.4, there is a zero in the beam-end frequency response function at 60.3 rad/s. At this frequency, there is very little motion at the end of the beam, thus facilitating sliding of the frictional interface and maximizing the work done by the

friction force. At 28.6 rad/s, some of the energy is transferred to the 2nd mode of beam via stick-slip motion. Although there is a slight increase in the energy dissipated by the modal damping of the beam, the energy dissipation provided by the friction damping is still dominant, especially given the small modal damping ratios used in this study. Another way to interpret these results is by examining the controllability of the beam-mass system.

4.3.2 Controllability of the Beam-Mass System

Controllability is defined as the ability of an input to transfer the state vector of a system from any initial value to any final value in finite time [41]. In other words, controllability is a measure of whether or not the state-space equation can be controlled from the input. In the case of the beam-mass system, there is no "control input" *per se*, but we are interested to know the degree to which the friction force acting between the beam's end and the mass m_2 can effectively remove energy from the system. Treating the friction force as a control input, and setting the external disturbance $P(t)$ to zero, equation (4.12) reduces to

$$\{\dot{q}\} = [A]\{q\} + \{B\}F \tag{4.29}$$

To investigate the controllability of (4.29), it is assumed that F can attain any functional form. In reality, however, it is limited in magnitude and can only oppose the relative motion during slip. Since (4.29) is linear and time-invariant, a simple test exists to determine controllability [41]. According to linear system theory, the system is controllable if and only if the controllability matrix, Λ, has full rank:

$$\Lambda = [B\ AB\ A^2B\ \ldots\ A^{n-1}B] \tag{4.30}$$

where n is the dimension of the state and input matrices, $n = 2(NM+1)$. Thus, (4.29) is controllable if and only if Λ has n linearly independent columns. Note that the first column of Λ is the input vector $\{B\}$, and each subsequent column amounts to $[A]$ times the previous column.

Initial attempts to compute Λ were unsuccessful because of numerical overflow/underflow problems, which were tied to the relative disparity in the size of the elements of the A matrix. To alleviate this problem, each column of the Λ matrix was normalized prior to multiplication by $[A]$. This operation alleviates the roundoff errors, while preserving the column space of the Λ matrix.

While the rank of Λ determines whether or not the system is controllable, the *degree to which the system is controllable* can be quantified by the condition number of Λ. The condition number of Λ can be defined by:

$$cond(\Lambda) = \left\|\Lambda\right\| \cdot \left\|\Lambda^{-1}\right\| = \sigma_{\max} / \sigma_{\min} \tag{4.31}$$

where σ_{max} and σ_{min} are the maximum and minimum singular values of Λ, respectively. If the columns of Λ are orthogonal, $cond(\Lambda) = 1$. As the linear independence of the columns of Λ degrades, the condition number of Λ will get larger and larger. If the columns of Λ become linearly-dependent, $cond(\Lambda) = \infty$, indicating a loss of rank. In practical terms, if $cond(\Lambda)$ is high, it indicates that high magnitudes of control force will be necessary to reach various points in the state space. This has increased significance in the beam-mass system under consideration because the control input in this case is the friction force, which has bounded magnitude.

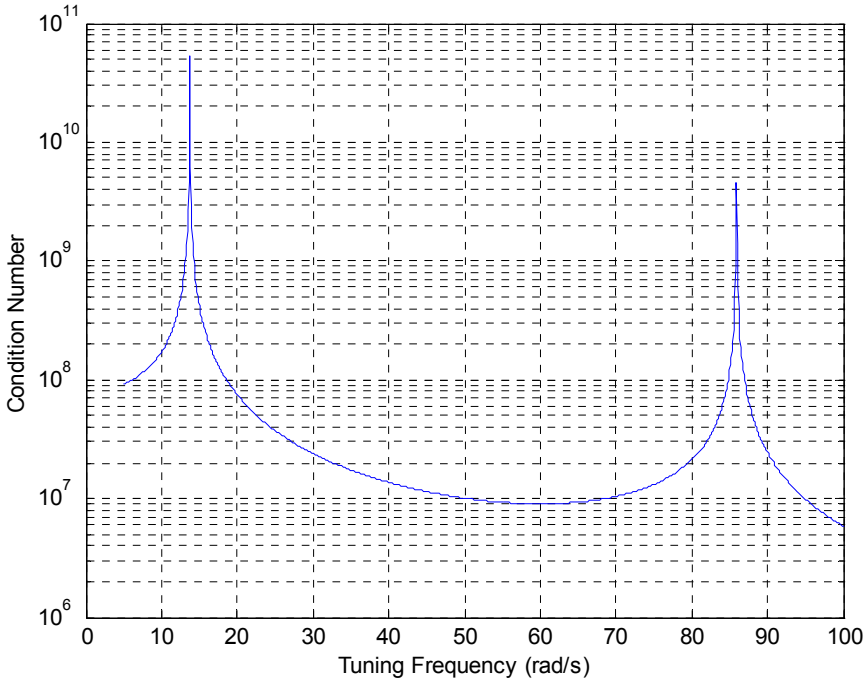

Figure 4.9. Condition number of the controllability matrix versus tuning frequency.

Figure 4.9 shows the condition number of Λ for tuning frequencies between 5 and 100 rad/s. Qualitatively, the figure shows relatively poor controllability when the tuning frequency coincides with a natural frequency of the beam. This indicates that it is more difficult for the friction force to affect the dynamics of the system at these tuning frequencies. Therefore, the friction force does less work and has poor energy dissipation capabilities. On the other hand, the condition number is lowest at a tuning frequency of 59.9 rad/s. At this frequency, the control input has the most control over the dynamics of the system; therefore, the friction force has the greatest potential to damp out the system response. The reason why 59.9 rad/s is associated with high energy dissipation can be found by looking at the phase angle in Figure 4.5. This frequency is just to the left of the zero phase angle associated with the zero at 60.3 rad/s. At 59.9 rad/s, the phase

difference between the response of beam and the input, coupled with the small response of the beam, contribute to high slip in the friction interface and maximizes the work done by the friction force. Similarly, frequencies just to the right of 60.3 rad/s can also contribute to high energy dissipation because of the phase difference.

For the most part, the controllability result is consistent with the results shown in Figure 4.8. However, controllability only applies to linear systems and this method cannot predict the nature of the system at the internal resonances. Furthermore, the friction force is not fully variable, but must follow the Stribeck relation given in (4.1). Only a full simulation of the nonlinear system can reveal the entire story. The next section describes the sensitivity of the nonlinearities to the tuning frequency and friction law.

4.4 Sensitivity of the Beam-Mass System

The previous section shows that energy dissipation is poor when the tuning frequency is near the beam frequencies and the best energy dissipation occurs when the beam and mass systems are mistuned. This behavior stands in contrast with that of the 3DOF system in Chapter 3. In Chapter 3, the best energy dissipation occurred when one of the subsystems was tuned to the natural frequency of another subsystem (or a harmonic thereof). This difference of results illustrates an important point – that the behavior of frictional systems is highly sensitive, and that results vary considerably depending on the system model. Therefore, this section explores the sensitivity of the energy dissipation results to the tuning parameter and the nature of the friction law.

4.4.1 Sensitivity to Tuning Parameter

To analyze the sensitivity of the energy results, a slice of the mesh in Figure 4.8 was examined. This slice, shown in Figure 4.10, is the total system energy remaining after 4.6 s of free response for a constant normal force of 10 N. The point of least energy remaining (or most energy dissipated) appears to be to the right of the zero at 60.3 rad/s. Displayed on a semi-log scale, Figure 4.10 appears very noisy, especially at low energy levels. To determine whether this feature was an artifact of the simulation method or an actual characteristic of the system, the time histories at different tuning ratios were examined.

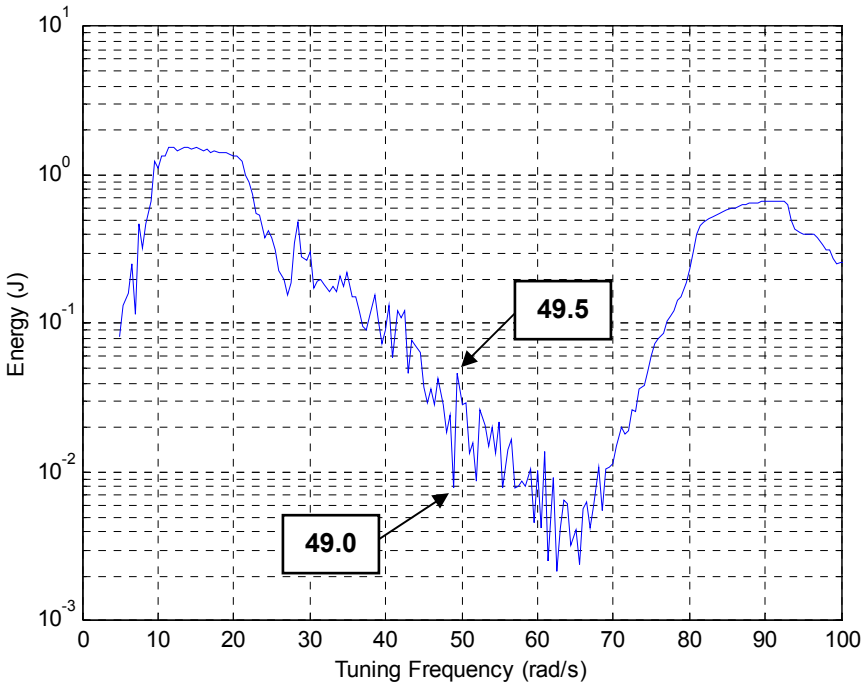

Figure 4.10. Total system energy as a function of tuning frequency for $N = 10$ N.

The time histories of two adjacent points at tuning frequencies of 49.0 and 49.5 rad/s were studied. These points were selected because there is a relatively large difference in energy between them (see Figure 4.10). Figure 4.11 shows the time histories of the relative displacements between the end of the beam ($x = L$) and the attached mass for the two tuning frequencies. From this plot, it is evident that a noticeable difference in the time response of the system exists despite the fact that only one system parameter was varied slightly. The difference between a system with a tuning frequency of 49.0 rad/s versus 49.5 rad/s is a 2% increase in the spring stiffness, k_2. Figure 4.11 also shows why there is more energy remaining at 49.5 rad/s than at 49.0 rad/s. For a tuning frequency of 49.5 rad/s, the relative displacement is constant beyond $t = 1.5$ s, indicating that the friction interface becomes stuck. However, when the tuning parameter is set to 49.0 rad/s, the friction interface goes through another half-cycle of stick-slip before becoming completely stuck, thereby dissipating more energy.

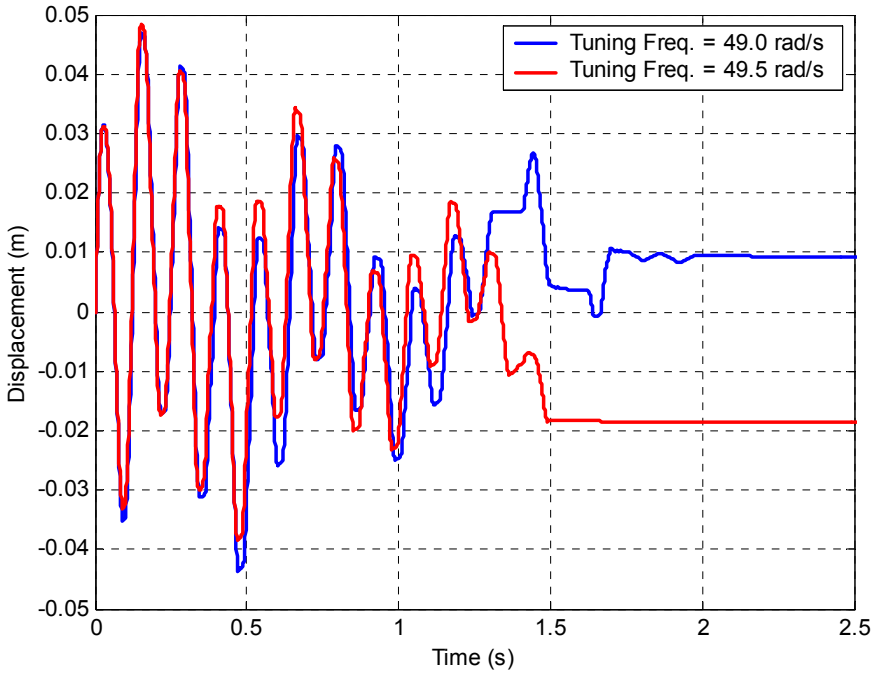

Figure 4.11. Relative displacement versus time for two tuning frequencies.

4.4.2 Sensitivity to Friction Laws

Although the Stribeck friction model is used in this case, it is instructive to see how the system behavior changes with differences in the friction law characteristics. The cases that were evaluated were an equivalent viscous damper and a frictional interface with a simple Coulomb friction law. The friction force for the Coulomb law is exactly as is given by (4.1), except that the coefficient of friction is constant with slip velocity. For this analysis, the friction coefficient of the Coulomb model is equal to the dynamic friction coefficient of the Stribeck law. These cases were chosen because they represent more simple models of a frictional interface.

The value of the equivalent viscous damper can be derived from expressions of energy dissipated over one cycle of motion [21]. The purpose is to identify a viscous

damping constant that approximates the energy loss per cycle by a friction damper. Assuming harmonic motion, the energy dissipated by the viscous damper is equated to the energy dissipated by a friction damper over one period. The energy dissipated by a viscous damper, $(E_{dis})_{vis}$, over one cycle of oscillation is given by

$$(E_{dis})_{vis} = \int_0^{(2\pi/\omega)} c_{eq}\dot{y}^2 dt \tag{4.32}$$

where c_{eq} is the damper constant, ω is the frequency of oscillation, and y is the assumed harmonic displacement with amplitude Y and frequency ω. Therefore, the time derivative of y is

$$\dot{y} = Y\omega\cos(\omega t). \tag{4.33}$$

Substituting (4.33) into (4.32) and integrating results in

$$(E_{dis})_{vis} = c_{eq}Y^2\omega^2 \int_0^{(2\pi/\omega)} \cos^2(\omega t)dt = c_{eq}Y^2\omega\pi. \tag{4.34}$$

The energy dissipated over one cycle by a friction damper can be shown to be

$$(E_{dis})_{fric} = 4Y\mu N, \tag{4.35}$$

therefore, equating (4.35) and (4.36) and solving for c_{eq} results in

$$c_{eq} = \frac{4\mu N}{\pi\omega Y}. \tag{4.36}$$

From (4.36), the damping constant is a function of the frequency and amplitude of motion. In this case, the viscous damper was chosen to approximate the damping done by the friction damper when the tuning frequency is at 13.7 rad/s. The friction coefficient used was the dynamic coefficient.

The system energies remaining after 4.6 s of free response are compared in Figure 4.12 for the viscous damping, Coulomb, and Stribeck cases. From this plot, two

differences between the viscous and the friction dampers are apparent. First, the peaks corresponding to excitation of the beam modes are much more narrow for the viscous damper case than the friction cases. The broad peaks in the friction cases are due to the saturation-like feature discussed in Section 4.2.2. Secondly, unlike the friction dampers, the system with the viscous damper shows no pronounced minimum near a tuning parameter of 60.0 rad/s.

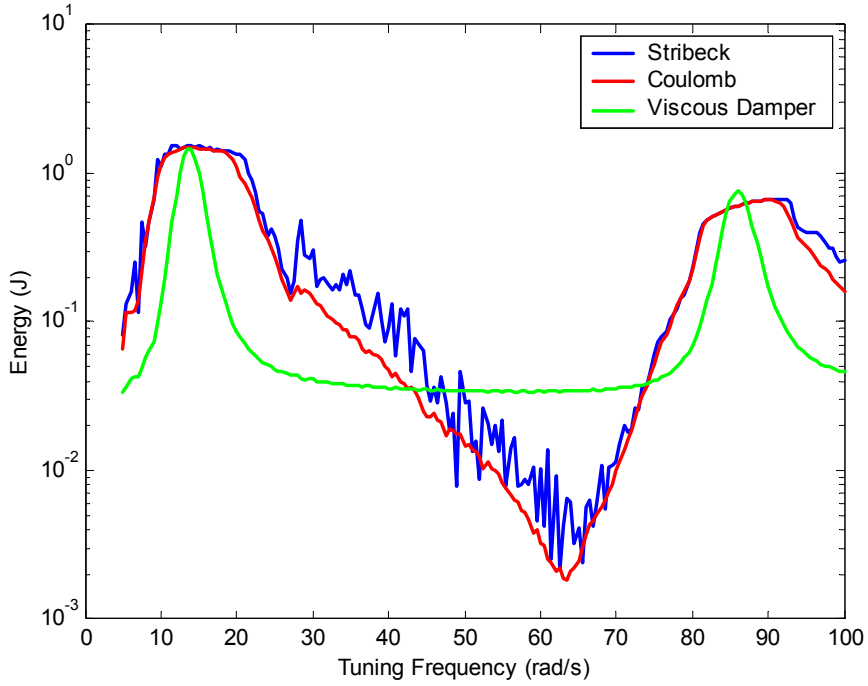

Figure 4.12. Total energy remaining after 4.6s versus tuning frequency for different friction laws.

The differences between the dry friction laws are more subtle. In the vicinity of the peaks, the two friction laws agree well. However, as the energy decreases, the Stribeck case fluctuates much more than the Coulomb case. This lack of fluctuations in the Coulomb case is due to the constant friction coefficient, which allows for sticking to

take place more consistently as the tuning parameter is varied. In the Stribeck case, the friction coefficient changes rapidly when the velocity is small, therefore, the point when the friction interface sticks is more sensitive to changes in the system. Furthermore, since the friction coefficient for the Coulomb case is the dynamic coefficient (which is smaller than the static coefficient), more sliding is allowed, thus more energy is dissipated. Lastly, the Stribeck case picks up the effects of the internal resonance at 28.6 rad/s, as seen by a spike at this frequency in Figure 4.12. However, any indication that an internal resonance is present in the Coulomb case is negligible.

As the results show, the behavior of the beam-mass system varies greatly with system parameters. In particular, the complexity of the frictional interface significantly affects the dissipated energy. For some applications, using a viscous damper to approximate a frictional interface may be appropriate. However, accurate simulations of precision space structures (as discussed in Chapter 1) require greater modeling detail. The Stribeck model revealed dynamics and mechanisms of energy transfer that the other methods did not exhibit. Certainly, the Stribeck model is not the best friction model by any means. The purpose of this study was not to show that the Stribeck case is better than the others, but to show the importance of selecting an appropriate friction law to model a given system.

CHAPTER 5

SUMMARY AND CONCLUSIONS

The purpose of this thesis is to explore two aspects of modeling the behavior of joint friction in structures. The first aspect deals with the accurate and efficient simulation of a simple system that incorporates an advanced friction law. Energy transfer and dissipation in a structural joint model is the second topic of this thesis. Motivation for this study stems from the need to have accurate models of high-precision space structures. Because friction at connecting joints plays a major role in the dynamics of the structure, a good understanding of this mechanism is necessary to predict the vibratory response of the structure.

5.1 Summary

The nature of the friction law can have a significant impact on the behavior of a jointed structure. Good friction models are desirable to predict the dynamic response of a structure, and a wide variety of friction laws have been proposed to date. However, it is well known that frictional systems are numerically difficult to simulate. Chapter 2 addresses these issues by simulating a simple system with a frictional interface modeled using the LuGre friction law. The LuGre friction law is chosen because it incorporates many characteristics of other friction models. The main purpose of Chapter 2 is to analyze the dynamics of the frictional system and to determine the best and most efficient numerical method to simulate the system.

To analyze the behavior of the frictional system, a SDOF spring-mass system sliding against a fixed surface was considered. The equations of motion for this system were converted to a nondimensional form for convenience as well as to prevent round-off errors in the calculations. The spring-mass system was analyzed by observing the linearized dynamics of the entire system as well as the time constant of the LuGre model alone. The analysis showed that the friction dynamics can be very fast and therefore numerically stiff during periods of high slip velocity. Furthermore, the dynamics changed rapidly at stick-slip transitions. It was found that the system dynamics were relatively well-conditioned during periods of sticking, which stood in contrast to the standard behavior of other friction models.

To determine the best and most efficient simulation method for the SDOF system, explicit and implicit time integration methods were considered. In general, the explicit methods required smaller time steps than the implicit methods. Consequently, this requirement led to longer simulation times as well as a larger number of integration steps. However, the explicit methods performed better in terms of accuracy. Attempts to reduce the simulation time by varying the time steps performed poorly for both explicit and implicit methods. This poor performance was attributed to a slight time shift in the solution, which caused relatively large errors. The best simulation methods were found to be the explicit Runge-Kutta and implicit Radau-IIA methods with constant time steps of 10^{-3} and 10^{-2}, respectively. Determining which is the best method depended on one's need for better accuracy (Runge-Kutta) or reduced memory usage (Radau-IIA). However, when simulating a large dynamical system, using a larger time step would greatly reduce the computation time. This advantage outweighs improved accuracy

afforded by the Runge-Kutta method. Therefore, for large systems with LuGre friction, the Radau-IIA method is determined to be the best method for numerical integration.

Chapters 3 and 4 are concerned with the second topic of this thesis. This topic deals with the concepts of energy pumping and energy dissipation in a jointed structure. The hypothesis is that joint friction can be a means to pump low-frequency vibrational energy to high-frequency vibrational energy, through the action of stick-slip oscillations. Since energy can be dissipated faster at higher frequencies, this pumping of energy to excite higher resonances may serve as a tool for increased energy dissipation.

In Chapter 3, a discrete 3DOF system was used to model a jointed structure. To isolate the mechanism that caused stick-slip motion, the frictional interface was modeled using the Stribeck friction model. From numerical simulations of the steady-state forced and free responses, several aspects of the system were observed. In the case of harmonic excitation, the frictional interface produced a stick-slip response that excited internal resonances at odd harmonics of the driving frequency. Second, there was a one-way transfer of energy from one subsystem to the other. Finally, by studying the energies in the 3DOF system, it was shown that, depending on the tuning ratio, friction could pump energy from one frequency to higher frequencies. When the 3rd subsystem was tuned to be receptive to these higher frequencies, there was an increase in energy dissipation versus the case where friction was not present. This increase in energy dissipation could lead to an improved damping capacity of the overall system.

The investigation in Chapter 3 was admittedly simple in order to permit a more thorough understanding of the phenomenon. The subsystems were SDOF spring-mass-damper systems and the friction model was of the Stribeck type. In Chapter 4, the

concepts learned in Chapter 3 are applied to a more complicated, and realistic, jointed system. This model incorporates a continuous beam and a floating joint configuration. Furthermore, the multi-mode nature of the beam gives rise to more interesting dynamics.

The analyses done to the beam-mass system of Chapter 4 paralleled that of Chapter 3. The frequency response of the beam-mass system showed the presence of internal resonances. These resonances corresponded to the odd harmonics of the drive frequency coinciding with various modes of the beam. Similar to the energy study in Chapter 3, the energy dissipation of the beam-mass system was evaluated during the free response of the system. However, the result from this simulation was opposite of the results from Chapter 3. In this case, there was poor energy dissipation when the mass subsystem was tuned to the resonances of the beam. Even at the internal resonances, where energy was pumped to the higher modes of the beam, there was worse energy dissipation than when the system was completely mistuned. These surprising results were attributed to the fact that friction was much more efficient in dissipating energy than the modal damping in the beam. The results were also partially confirmed by looking at the controllability of the linear state-space system.

The difference in results between Chapters 3 and 4 demonstrates that the behavior of frictional systems is very sensitive to system parameters and to structural configuration. The last part of Chapter 4 shows that the energy dissipation of the system is sensitive to slight changes in the tuning parameter. Furthermore, the response of the system using the Stribeck model reveals many features that other, simpler friction models do not.

5.2 Conclusions and Future Work

Although this thesis is a preliminary study of the behavior of joint friction, it can provide a framework to accurately model and design jointed structures. For example, Chapter 2 presents an analysis of the numerical issues associated with the simulation of a frictional system. Results from this chapter could be useful in simulating a large structural system, especially if the system employs the LuGre friction model.

In Chapters 3 and 4, the models of the jointed structure are general and not specific to any joint geometry. In essence, they represent two structures connected by a frictional interface. This generalization could apply to different joint geometries such as sleeve or revolute joints. Results from Chapters 3 and 4 could lead to design guidelines to enhance energy dissipation in the system. For example, it is shown that friction indeed pumps energy to higher modes. Structural designers should take advantage of this phenomenon whenever possible in order to maximize the passive damping capacity of a system. However, difference in results between Chapters 3 and 4 demonstrates that frictional systems are sensitive to parameter changes, and that design rules will often be application-specific. Lastly, the sensitivity of observed results to friction laws and system tuning reinforces the need to model a system with the appropriate level of detail.

In reality, however, the behavior of a jointed structural system is a large puzzle with many pieces. Many variables and nonlinearities contribute to the actual behavior of such a system. The results of this thesis provide a clue to one of those puzzle pieces.

A natural extension of this thesis is to apply the LuGre friction model to the joint models in Chapters 3 and 4, as well as more complicated structural systems. Furthermore, future studies could employ more complicated friction models as well as

attempt to quantify the contribution of joint friction to the damping of a structural system. Finally, it is important to experimentally study and validate the simulated behavior found in this study. Ultimately, observations of space-deployed structures are needed to confirm the predictions of numerical simulations.

REFERENCES

[1] Dubowsky, Steven, "Dealing With Vibrations in the Deployment Structures of Space Robotic Systems," *5th International Conference on Adaptive Structures*, Sendai, Japan, December 5-7, 1994.

[2] NASA Fact Sheet, FS-1996-08-09-LaRC, August, 1996.

[3] Lake, Mark S., Lee D. Peterson, M. Roman Hachkowski, Jason D. Hinkle, and Lisa R. Hardaway, "Research on the Problem of High-Precision Deployment for Large-Aperture Space-Based Science Instruments," *Space Technology and Applications International Forum*, Albuquerque, New Mexico, January 25-29, 1998.

[4] Warren, Peter A., "Sub-Micron Non-Linear Shape Mechanics of Precision Deployable Structures," Ph.D. Dissertation, University of Colorado, Boulder, 1996.

[5] Silver, Mark J., Lee D. Peterson, and Lisa M.R. Hardaway, "Picometer Scale Spontaneous Vibrations in a Deployable Boom Under Thermal Loading," *42nd Structures, Structural Dynamics and Materials Conference*, Seattle, Washington, April 16-19, 2001.

[6] Hardaway, Lisa M.R. and Lee D. Peterson, "Nanometer Scale Spontaneous Vibrations in a Deployable Truss Under Mechanical Loading," *42nd Structures, Structural Dynamics and Materials Conference*, Seattle, Washington, April 16-19, 2001.

[7] Ungar, E.E., "The Status of Engineering Knowledge Concerning the Damping of Built-up Structures," *Journal of Sound and Vibration*, vol. 26, pgs. 141-154, 1973.

[8] Beards, C.F., "Damping in Structural Joints," *The Shock and Vibration Digest*, vol. 24, pgs. 3-7, 1992.

[9] Ferri, A.A. and B.S. Heck, "Analytical Investigation of Damping Enhancement Using Active and Passive Structural Joints," *AIAA Journal of Guidance, Control, and Dynamics*, vol. 15, no. 5, pgs. 1258-1264, 1992.

[10] Gaul, L. and R. Nitsche, "Friction Control for Vibration Suppression," *Mechanical Systems and Signal Processing*, vol. 14, no. 2, pgs. 139-150, 2000.

[11] Gaul, L. and R. Nitsche, "The Role of Friction in Mechanical Joints," *Applied Mechanics Reviews*, vol. 54, pgs. 93-105, 2001.

[12] Folkman, S.L. and F.J. Redd, “Gravity Effects on Damping of a Space Structure with Pinned Joints,” *AIAA Journal of Guidance, Control, and Dynamics*, vol. 13, pgs. 228-233, 1990.

[13] Folkman, S.L., E.A. Rowsell, and G.D. Ferney, “Influence of Pinned Joints on the Damping and Dynamic behavior of a Truss,” *AIAA Journal of Guidance, Control, and Dynamics*, vol. 18, pgs. 1398-1403, 1995.

[14] Hertz, T.J. and E.F. Crawley, “Displacement Dependent Friction in Space Structural Joints,” *AIAA Journal*, vol. 23, pgs. 1998-2000, 1985.

[15] Ferri, Aldo A., “Modeling and Analysis of Nonlinear Sleeve Joints at Large Space Structures,” *AIAA Journal of Spacecraft and Rockets*, vol. 25, pgs. 354-360, 1988.

[16] Armstrong-Hélouvry, B., P. Dupont, and C. Canudas de Wit, "A Survey of Models, Analysis Tools and Compensation Methods for the Control of Machines with Friction," *Automatica*, vol. 30, no. 7, pgs. 1083-1138, 1994.

[17] Mitiguy, P.C. and A.K. Banerjee, “Efficient Simulations of Motion Involving Coulomb Friction,” *AIAA Journal of Guidance, Control, and Dynamics*, vol. 22, no. 1, January-February, pgs. 78-86, 1999.

[18] Pfeiffer, F. and C. Glocker, *Multibody Dynamics with Unilateral Contact*, John Wiley and Sons, 1996.

[19] Ferri, A.A., and B.S. Heck, "Analysis of Stick-Slip Motion in Coulomb Damped Systems Using Variable Structure System Theory," *Proceedings of the 1997 ASME Design and Technical Conferences*, Sacramento, CA, September 14-17, 1997

[20] Whiteman, W.E. and A.A. Ferri, "Multi-Mode Analysis of Beam-Like Structures Subjected to Displacement-Dependent Dry Friction Damping," *Journal of Sound and Vibration*, vol. 201, no. 3, pgs. 403-418, 1997.

[21] Ferri, A.A., "Friction Damping and Isolation Systems," *ASME Journal of Vibration and Acoustics*, vol. 117B, June, pgs. 196-206, 1995.

[22] Dahl, P.R., “Solid friction damping of mechanical vibrations”, *AIAA Journal*, vol. 14, pgs. 1675-1682, 1976.

[23] Gaul, L., J. Lenz, and D. Sachau, “Active Damping of Space Structures by Contact Pressure Control in Joints,” *Mechanical Structures and Machines*, vol. 26, no. 1, pgs. 81-100.

[24] Valanis, K.C., 1971, “A Theory of Viscoplasticity Without a Yield Surface,” *Archives of Mechanics*, vol. 23, no. 4, pgs. 171-191.

[25] Swevers, J., F. Al-Bender, C.G. Ganesman, and T. Prajogo, “An Integrated Friction Model Structure with Improved Presliding Behavior for Accurate Friction Compensation,” *IEEE Transactions on Automatic Control,* vol. 45, no. 4, April, pgs. 675-686, 2000.

[26] Lampaert, V., J. Swevers, and F. Al-Bender, “Modification of the Leuven Integrated Friction Model Structure,” *IEEE Transactions on Automatic Control,* vol. 47, no. 4, April, pp. 683-687, 2002.

[27] Haessig, D.A., Jr. and B. Friedland, “On the modeling and simulation of friction”, *ASME Journal of Dynamic Systems, Measurement, and Control*, vol. 113, pgs. 354-362, 1991.

[28] Canudas de Wit, C., H. Olsson, K.J. Astrom, and P. Lischinsky, "A New Model for Control of Systems with Friction," *IEEE Transactions on Automantic Control,* vol. 40, no. 3, pgs. 419-425, 1995.

[29] Gendelman, O., L.I. Manevitch, A.F. Vakakis, and R. M’Closkey, “Energy Pumping in Nonlinear Mechanical Oscillators: Part I – Dynamics of the Underlying Hamiltonian Systems,” *ASME Journal of Applied Mechanics*, vol. 68, pgs. 34-41, 2001.

[30] Onoda, Junjiro, Tetsuji Sano, and Kenji Minesugi, “Passive Vibration Suppression of Truss by Using Backlash,” *The 34th AIAA/ASME/ASCE/AHS/ASC Structures, Structural Dynamics, and Materials Conference*, La Jolla, CA, April 19-22, 1993.

[31] Ferri, A.A. and E. H. Dowell, “Frequency Domain Solutions to Multi-Degree-of-Freedom, Dry Friction Damped Systems,” *Journal of Sound and Vibration*, vol. 124, no. 2, pgs. 207-224, 1988.

[32] Kokotovic, P., H. Khalil, and J. O’Reilly, *Singular Perturbation Methods in Control: Analysis and Design*, Academic Press, London, 1986.

[33] Forsythe, G., M. Malcolm, and C. Moler, *Computer Methods for Mathematical Computations*, Prentice-Hall, New Jersey, 1977.

[34] Kahaner, D., C. Moler, and S. Nash, *Numerical Methods and Software*, Prentice-Hall, New Jersey, 1989.

[35] Faires, J.D. and R. Burden, *Numerical Methods, 2nd Edition*, Brooks/Cole Publishing Co., Pacific Grove, CA, 1998.

[36] Hairer, E. and G. Wanner, *Solving Ordinary Differential Equations II: Stiff and Differential-Algebraic Problems*, Springer-Verlag, Berlin, 1991.

[37] Bindemann, A.C., and A.A. Ferri, "The Influence of Friction Models on the Passive Damping and Dynamic Response of a Flexible Beam Structure," *Proceedings of the 36th AIAA/ASME/ASCE/AHS/ASC Structures, Structural Dynamics, and Materials Conference*, New Orleans, LA April 10-12, pgs. 180-189, 1995.

[38] Ibrahim, R.A., "Friction Induced Vibration, Chatter, Squeal, and Chaos: Part I – Mechanics of Friction," *Applied Mechanics Reviews*, vol. 47, no. 7, pgs. 209-253, 1994.

[39] Nayfeh, Ali Hasan, and Dean T. Mook, *Nonlinear Oscillations*, John Wiley and Sons, New York, 1979.

[40] Ginsberg, Jerry H., *Mechanical and Structural Vibrations*, 1st ed., John Wiley and Sons, New York, 2001.

[41] Chen, Chi-Tsong, *Linear System Theory and Design*, 3rd ed., Oxford University Press, New York, 1999.